Peroxisome deficiency underlies failures in hepatic immune cell development and antigen presentation in a severe Zellweger disease model

Brendon Parsons, Daniel Medina-Luna, Michal Scur, Marinella Pinelli, Gayani Gamage, Rebecca Chilvers, Yannick Hamon, Ibrahim H.I. Ahmed, Stéphane Savary, Stéphane Savary, et al.

Cell Reports

Article

Peroxisome deficiency underlies failures in hepatic immune cell development and antigen presentation in a severe Zellweger disease model

Graphical abstract

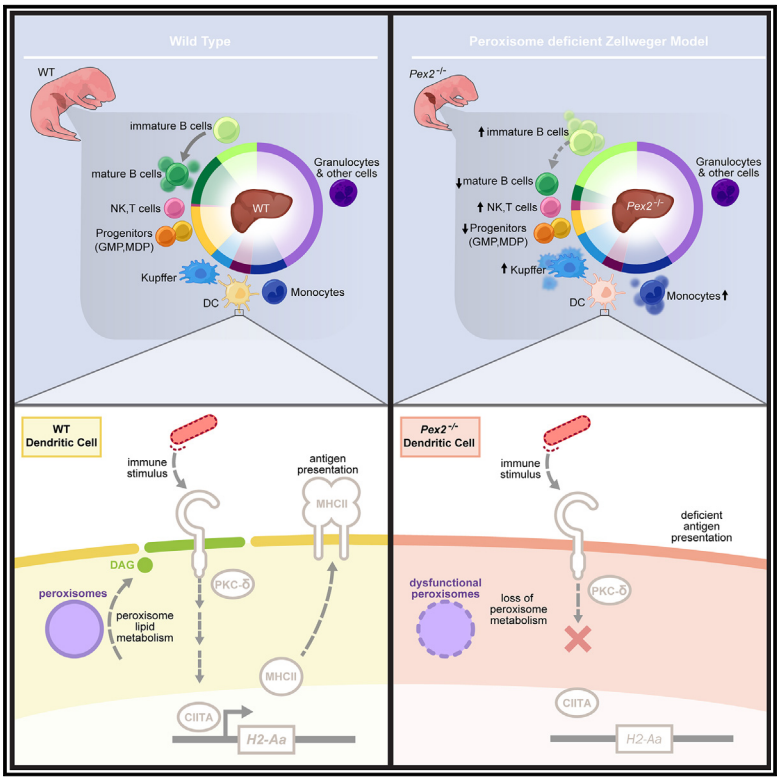

Highlights

- Peroxisomes are required for developmental hematopoiesis in mouse
- PBD-ZSS murine model has defects in B cell, granulocyte, and cDC development
- Peroxisomal DAG in DC regulates PKC-δ-mediated expression of MHC class II
- Hematopoietic defects may be a feature of PBD-ZSS spectrum

Authors

Brendon D. Parsons, Daniel Medina-Luna, Michal Scur, ..., Eicke Latz, Tobias K. Karakach, Francesca Di Cara

Correspondence

dicara@dal.ca

In brief

Parsons et al. report that peroxisomes are required for hepatic hematopoiesis. They found hematopoietic defects in granulocytes, dendritic cells, and B cells of *Pex2*$^{-/-}$ Zellweger syndrome mice. Finally, they demonstrated that peroxisomes control the diacylglycerol-mediated activation of PKC-δ to drive MHC class II expression for effective antigen presentation to CD4^{+} T lymphocytes.

Parsons et al., 2024, Cell Reports *43*, 113744
February 27, 2024
https://doi.org/10.1016/j.celrep.2024.113744

CellPress

Cell Reports

CellPress
OPEN ACCESS

Article

Peroxisome deficiency underlies failures in hepatic immune cell development and antigen presentation in a severe Zellweger disease model

Brendon D. Parsons,[1,9] Daniel Medina-Luna,[2,9] Michal Scur,[2] Marinella Pinelli,[2] Gayani S. Gamage,[2] Rebecca A. Chilvers,[2] Yannick Hamon,[3] Ibrahim H.I. Ahmed,[4,8] Stéphane Savary,[5] Andrew P. Makrigiannis,[2,8] Nancy E. Braverman,[6] Juan F. Rodriguez-Alcazar,[7] Eicke Latz,[7] Tobias K. Karakach,[4,8] and Francesca Di Cara[1,8,10,*]

[1]University of Alberta, Department of Laboratory Medicine and Pathology, Edmonton, AB T6G 1C9, Canada
[2]Dalhousie University, Department of Microbiology and Immunology, Halifax, NS B3K 6R8, Canada
[3]Aix Marseille University, CNRS, INSERM au Centre d'Immunologie de Marseille Luminy, 13288 Marseille, France
[4]Dalhousie University, Department of Pharmacology, Halifax, NS B3H 4R2, Canada
[5]University of Bourgogne, Laboratoire Bio-PeroxIL EA7270, Dijon, France
[6]Research Institute of the McGill University Children's Hospital, Montreal, QC H4A 3J1, Canada
[7]University of Bonn, Institute of Innate Immunity, Medical Faculty, 53127 Bonn, Germany
[8]Beatrice Hunter Cancer Research Institute, Halifax, NS, Canada
[9]These authors contributed equally
[10]Lead contact
*Correspondence: dicara@dal.ca
https://doi.org/10.1016/j.celrep.2024.113744

SUMMARY

Peroxisome biogenesis disorders (PBDs) represent a group of metabolic conditions that cause severe developmental defects. Peroxisomes are essential metabolic organelles, present in virtually every eukaryotic cell and mediating key processes in immunometabolism. To date, the full spectrum of PBDs remains to be identified, and the impact PBDs have on immune function is unexplored. This study presents a characterization of the hepatic immune compartment of a neonatal PBD mouse model at single-cell resolution to establish the importance and function of peroxisomes in developmental hematopoiesis. We report that hematopoietic defects are a feature in a severe PBD murine model. Finally, we identify a role for peroxisomes in the regulation of the major histocompatibility class II expression and antigen presentation to $CD4^+$ T cells in dendritic cells. This study adds to our understanding of the mechanisms of PBDs and expands our knowledge of the role of peroxisomes in immunometabolism.

INTRODUCTION

Peroxisomes are essential metabolic organelles present in virtually every eukaryotic cell. In mammals, peroxisomes are the cellular compartments where unique lipid metabolic processes occur, such as β-oxidation of very-long-chain fatty acids (VLCFAs), α-oxidation of fatty acids, and synthesis of ether lipids.[1,2] Peroxisomes also regulate the synthesis and turnover of reactive oxygen and nitrogen species and contribute to the metabolism of polyamines, carbohydrates, and amino acids, making this organelle an essential regulator of cellular metabolism.[1] Peroxisome biogenesis, fission, and maturation through the import of proteins into the peroxisome matrix depend on a set of peroxin (PEX) proteins.[3] Mutations in the genes encoding PEX proteins impair peroxisome biogenesis and function and underlie a clinical spectrum of disorders known as peroxisome biogenesis disorders (PBDs).

PBDs are divided into two distinct syndromes: the Zellweger syndrome spectrum (PBD-ZSS) and the rhizomelic chondrodysplasia punctata spectrum (PBD-RCDP). Except for the *Pex7* mutation underlying most cases of PBD-RCDP, most other *Pex* gene mutations result in generalized peroxisome dysfunction and the PBD-ZSS phenotype.[4] The metabolic dysfunctions that arise in PBD-ZSS often affect the development of multiple organs, including the brain, liver, kidneys, and muscles.

Atypical phenotypes have recently been described for these phenotypic groups, indicating that the full spectrum of these disorders remains to be identified. For instance, case studies described patients with PBD-ZSS presenting defects in T cell differentiation.[5] The patients exhibited thymic hypoplasia and poorly developed T cell-dependent zones in all examined lymph nodes and spleen. One patient was affected by sepsis and died after 7 months of pneumonitis. Recently, a case of a newborn patient with PBD-ZSS who died of gram-negative fulminant sepsis was reported.[6] The infant had a low total white blood cell count, particularly neutrophils. Additionally, a case study of a 2-month-old infant with PBD-ZSS who presented with lymphopenia, thymic atrophy, and several recurrent opportunistic infections has been described.[7]

Although these studies demonstrate that a link exists between peroxisome function and the development and function of immune cells and that the poor prognoses of patients with PBD-ZSS are partly a consequence of defective immune development that results in infectious respiratory morbidity and sepsis, to date, no study has globally analyzed the role of peroxisomes on hematopoiesis in severe PBD-ZSS. Over the past 15 years, evidence has supported the hypothesis that peroxisomes are organelles of immunometabolism and that their activity can regulate different aspects of immunity in health and disease.[8] Peroxisome-derived ether lipids are required for neutrophil survival and development in mice.[9] These findings could partly explain why some patients with PBD-ZSS present with neutropenia. A requirement for ether lipids in the education, differentiation, and maturation of invariant natural killer T (iNKT) cells in the thymus has also been reported.[10] Moreover, peroxisomes have been directly linked to specific functions in innate and adaptive immune cells such as phagocytosis,[11] cytokine release,[12–15] and the production of immunoglobulin M (IgM) by innate B cells.[16] Thus, both clinical case studies and studies in animal models suggest that immune disorders could be a feature of PBD-ZSS.

The *Pex2* homozygous (*Pex2*$^{-/-}$) null mouse is a useful murine model of severe PBD-ZSS. *Pex2*$^{-/-}$ mice carry an insertion or deletion mutation in the gene that encodes for Pex2, a ubiquitin ligase,[17] that, if mutated, affects the import of peroxisomal enzymes into the matrix, leading to peroxisome biogenesis defects.[3] The *Pex2*$^{-/-}$ murine mouse was previously described[18] and showed canonic neurodevelopmental phenotypes typical of PBD-ZSS. Moreover, our recent study reported that *Pex2*$^{-/-}$ bone marrow-derived macrophages (BMDMs) exhibit defects in phagocytosis and inflammatory cytokine secretion upon stimulation with pathogens.[12]

To provide a more comprehensive study of the hematopoietic defects caused by peroxisomal deficiency that may underlie the observed immune disorders of PBD-ZSS, we performed a global examination of immune cell development in the liver of a *Pex2*$^{-/-}$ model of PBD-ZSS using single-cell RNA sequencing (scRNA-seq). The liver is the main hematopoietic organ during gestation and a reservoir for developing immune cells for almost a week after birth.[19,20] Our results demonstrated that *Pex2*$^{-/-}$ PBD-ZSS mice have hematopoietic defects detectable in myeloid and lymphoid cells. Additionally, we demonstrated that peroxisome metabolism is required for the activation of protein kinase C-δ (PKC-δ) to drive major histocompatibility complex class II (MHC class II) surface expression on dendritic cells (DCs) for effective antigen presentation to CD4^{+} T lymphocytes. This study defines immunometabolic requirements for peroxisomes in DCs and in regulating antigen presentation, an event that has an implication also for the activation of adaptive immunity.

RESULTS

Hepatic immune cell atlas of WT and *Pex2*$^{-/-}$ mice at single-cell resolution

To map the hepatic immune cell landscape in a neonatal Zellweger murine model, we isolated CD45^{+} cells from livers dissected from wild-type (WT), *Pex2* heterozygous (*Pex2*^{Het}), and *Pex2*$^{-/-}$ null mutant mice at postnatal day 0 and prepared these cells for scRNA-seq (Figure 1A). Although some of the *Pex2*$^{-/-}$ homozygous mice were reported to survive up to 15 days postbirth,[21] in our hands, *Pex2*$^{-/-}$ homozygous mice were lethal with high expressivity and penetrance after postnatal day 0, and therefore we used this time point in our study to capture the developmental defects that persist after birth. We focused on the liver because it is the major hematopoietic tissue at this developmental stage and can better reveal the effect that peroxisome dysfunction might have on the immune system of patients with Zellweger. The distribution of each genotype in the clustering of CD45^{+} day 0 mouse liver cells is represented using dimensional reduction by uniform manifold approximation and projection (Figure 1B). The expression of the *Pex2* transcript across these clusters is relatively universal in the hepatic immune subsets of WT and *Pex2*^{Het} mice and is completely abolished in *Pex2*$^{-/-}$ mice (Figure 1C). To assign cell-type classifications to our scRNA-seq results, we used two-dimensional hierarchical clustering across the most variable genes and used lists of cell-type markers from related scRNA transcriptomics and developmental studies of hepatic immune cell types[19,20,22–26] to annotate cell types (Figure 1D and S1A; Tables S1 and S2). Our scRNA-seq results show distinct transcriptional profiles consistent with 19 different immune cell populations, which can be clustered in subpopulations that express markers typical of fully differentiated cells or of cells still in differentiation or features of stemness and exhibit immune expression profiles largely similar to those previously reported in the mouse neonatal liver immune cells (Figures 1D, 1E, and S1B).[19,20] Neutrophils, B cell lineages, monocytes, and myeloid subsets of DCs and Kupffer cells comprised most of the immune cells present in the neonatal livers of WT, *Pex2*^{Het}, and *Pex2*$^{-/-}$ mice. Small clusters of cells with NK (natural killer)/T cell-like expression, basophils, erythroid lineages, and megakaryocytes are also identifiable in each genotype (Figure 1E).

The subclustering of major immune cell subsets allowed us to further define distinct subpopulations of developing hematopoietic cells, including clusters with gene signatures that resemble granulocyte monocyte progenitor (GMP) cells[20] and monocyte-DC progenitors (MDPs) (Table S2).[20,27–31] The GMP population clustered together with immature neutrophil (iNP) and monocyte populations, two lineages that arise from GMP differentiation, and MDPs clustered closely with DCs and monocytes, reflecting their developmental association with these lineages (Figure 1E). Similarly, we examined the neutrophil cluster and identified gene signatures consistent with previously reported developmental stages of mature neutrophils (mNPs), which show high expression of *Mmp9, Arg2*, and *Retnlg*; intermediate mNPs, which exhibit high expression of granule protein encoding genes *Ltf* and *Ngp*; and immature iNPs, which express *Cebpe* and *Camp* but also display overlapping expression profiles with GMP cells, with the expression of *Elane* and *Mpo*. Each of these neutrophil clusters also exhibited an expression of markers of activation such as *Cd177* and *S100a8/a9*,[32] a phenotype reported for neutrophilic lineages in the neonatal liver.[18] The monocyte population was found to express monocyte-associated genes such as *Vcan*[31] and *Fn1*[33] and monocyte/macrophage-associated genes *Fcgr1* and *Csfr1*. We also identified a very small

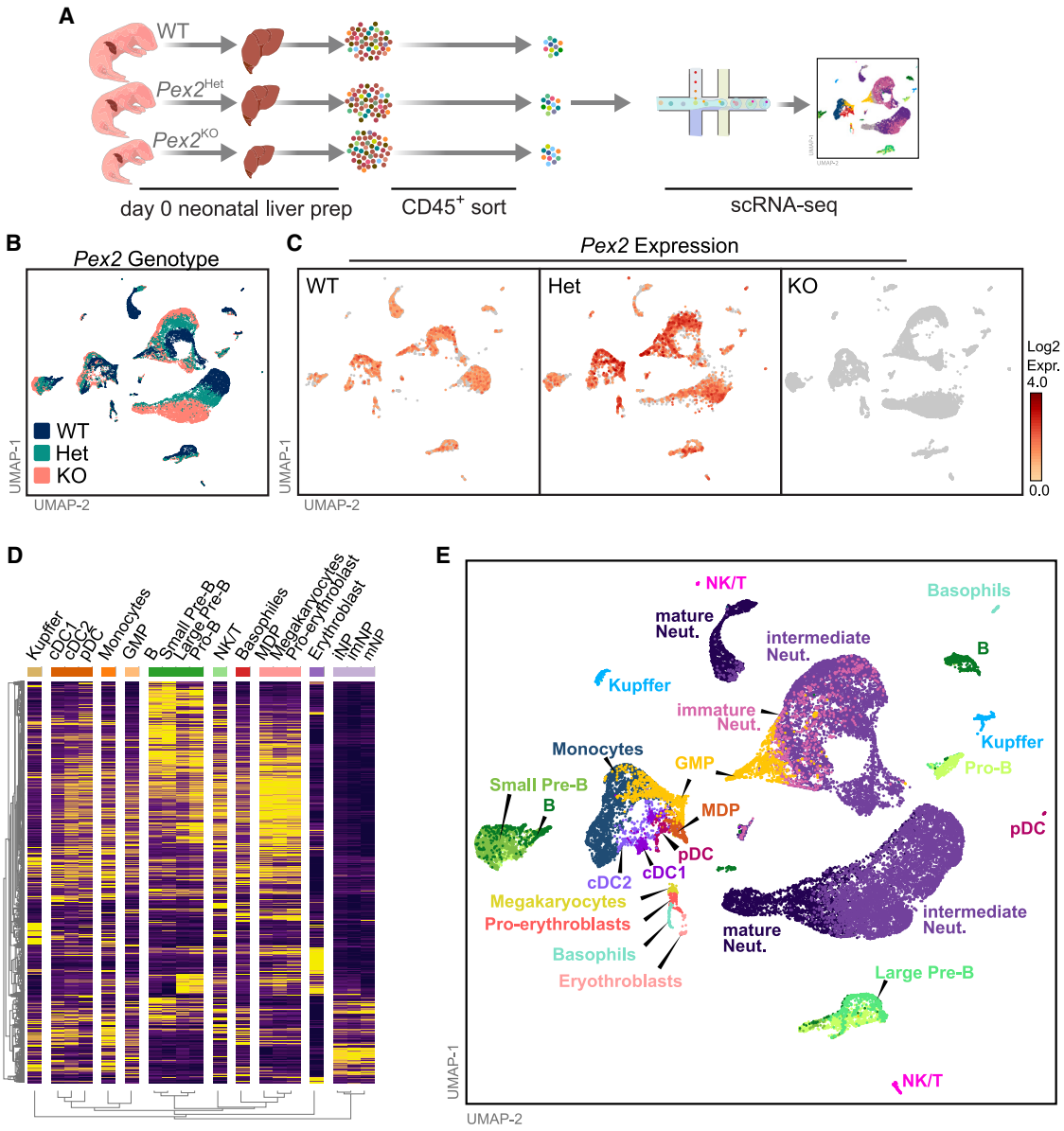

Figure 1. Transcriptional profiling of hepatic immune cell subsets of neonatal WT, *Pex2*^{Het}, and *Pex2*$^{-/-}$ mouse livers

(A) Diagram of the experimental pipeline of the single-cell analysis.

(B) Uniform manifold approximation and projection (UMAP) clustering of the integrated datasets representing the identified cellular clusters and cell types of the hepatic immune cells of WT, *Pex2*^{Het}, and *Pex2*$^{-/-}$ mice.

(C) Distribution of *Pex2* expression across UMAP clusters of WT, *Pex2*^{Het}, and *Pex2*$^{-/-}$ mice.

(D) Heatmap of select differential genes used to identify cluster types across all identified cells.

(E) Cell-type annotation of UMAP cluster of WT, *Pex2*^{Het}, and *Pex2*$^{-/-}$.

n = 2 mice per genotype.

See Figure S1 and Tables S1 and S2.

population of basophils by their expression of *Cd200r3*, *Prss34*, and *Cebpa*[34] (Figures 1E and S1A; Tables S1 and S2).

Analysis of the B cell population (*Cd19*-, *Rag1*-, and *Cd79a/b*-expressing cells) revealed several subpopulations, of which a majority in day 0 mice exhibited an immature expression profile of pro-B and large pre-B cells, with a prominent expression of IgM heavy chain, *Rag2*, and *Vpreb1* (Figures 1E and S1A; Tables S1 and S2). A subset of small pre-B cells could be distinguished from other subsets by the expression of *Fcmr*,[35] while mature B cells exhibited higher expression of *Bach2*.[36]

Also, although the liver is considered a lymphoid organ in adults and part of T cell development occurs in the liver of embryonic day 13-stage mice with T cell progenitors migrating to the thymus,[37] we found a residual pool of cells with NK/T cell-like

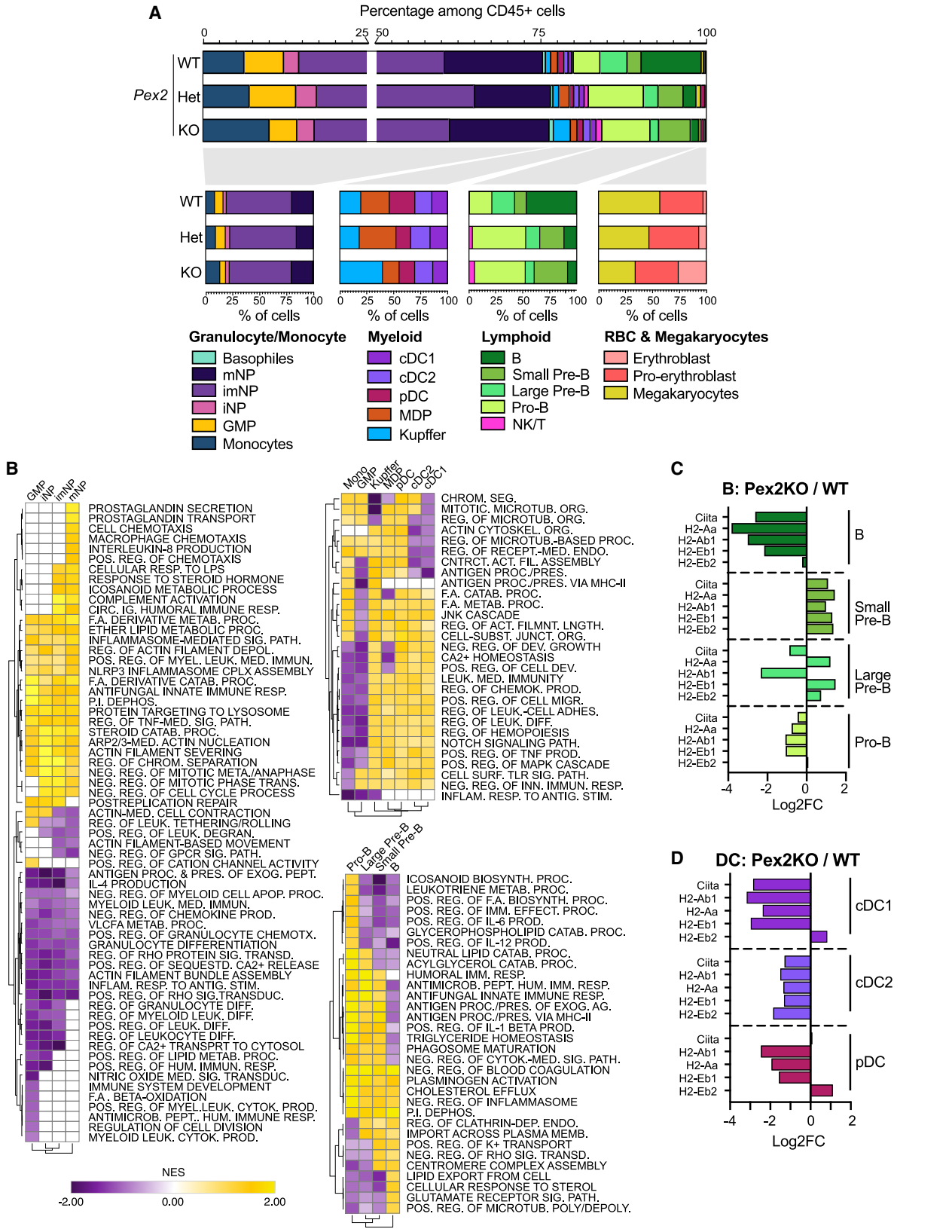

(legend on next page)

expression (*Ncr1*, *Klra5, Tbx21*, *Grzma*, *Grzmc*, *Fasl*) but that could not be individually distinguished as NK or T cells. Together, these data suggested that granulocytes, B cells, monocytes, and DCs are the most abundant immune cells in the neonatal hepatic immune environment.

We identified the conventional DC (cDC) populations cDC1 and cDC2 in the liver of all genotypes, with the distinct expression of genes such as *Itgae*, *Tlr11*, *Clec9a*, and *Cd74* in cDC1s and *Itgax*, *Batf3*, and *Ly6a* in cDC2s, as well as plasmacytoid DCs (pDCs) denoted by the expression of gene markers such as *Siglech*, *Klk1*, and Ccr9[38–40] (Figures 1E and S1A; Tables S1 and S2). The genes *Marco* and *Clec4f*[41] were highly expressed in Kupffer cells, a relatively small population of cells in the neonatal liver, which is not unexpected, as they are not as numerous as other cell types, and their presence increased a few days postbirth.[19]

Pex2$^{-/-}$ mice display compositional defects in the hepatic immune compartment

To determine if Pex2 plays a role in the development of any hepatic immune population, we assessed the proportion of each cell type identified in the scRNA-seq of neonatal mice of each genotype. Accounting for the difference in size of postnatal day 0 *Pex2*$^{-/-}$ mice with an average weight of 1 g compared to *Pex2*^{He} and WT (1.4 and 1.6 g, respectively) littermates, we observed a decrease in the proportion of B and large pre-B cells of both *Pex2*^{Het} and *Pex2*$^{-/-}$ mice compared to WT mice, representing the largest decrease in any cell population, which was contrasted by an increase in the pro-B and small pre-B populations (Figure 2A). Similarly, we observed a modest increase in the NK/T cell-like population in *Pex2*^{Het} and *Pex2*$^{-/-}$ mice. This shift in B cell numbers toward a larger immature B cell population in *Pex2*^{Het} and *Pex2*$^{-/-}$ mice suggests a dominant role for *Pex2* in B cell development. Assessing changes that are exclusive to the *Pex2*$^{-/-}$ mice, we observe a notable decrease in the proportion of GMPs and a greater proportion of Kupffer cells and monocytes in *Pex2*$^{-/-}$ compared to WT and *Pex2*^{Het} mice, and a stepwise increase in erythroblasts and a decrease in megakaryocytes was observed across WT, *Pex2*^{Het}, and *Pex2*$^{-/-}$ mice, while no trends in the changes in any other cell population were observed (Figure 2A).

Global GSEAs of the hepatic immune population reveal developmental and functional defects characteristic of peroxisomal dysfunction

To capture the overarching changes in the hepatic immune compartment of *Pex2*$^{-/-}$ mice, we mapped the network of the cellular processes found to be enriched among the differentially expressed genes of *Pex2*$^{-/-}$ compared to WT immune cells (Figures S2 and S3; Tables S3 and S4). We used differential gene expression analyses of genes in *Pex2*$^{-/-}$ compared to WT for each cell type, analyzed together or separately (Tables S3 and S5). Gene set enrichment analysis (GSEA) of the processes and pathways enriched from differentially expressed genes of *Pex2*$^{-/-}$ compared to WT revealed that mutation in *Pex2*$^{-/-}$ has effects on mitochondrial-associated processes such as oxidative phosphorylation, the citric acid and TCA cycles, the electron transport chain, and the ATP biosynthetic process and on processes associated with protein metabolism such as translation, purine metabolism, and cytoplasmic and mitochondrial ribosomal proteins (Figure S2A). These enrichments align with previously reported RNA-seq transcriptomic profiles of peroxisome dysfunction models in *Drosophila* and mice.[12,42] We also found that genes belonging to the amino acid catabolic processes and fatty acid β-oxidation were downregulated in *Pex2*$^{-/-}$ mice (Figure S2B), while genes encoding for enzymes of glycerophospholipid metabolism and glycolipid metabolism were upregulated in *Pex2*$^{-/-}$ mice (Figure S2B). Additionally, we found that a cellular network of processes associated with cortical actin cytoskeleton and Rho GTPase cycle regulation and MAPK signaling were enriched among genes that were upregulated in *Pex2*$^{-/-}$ immune cells (Figures S2C and S2D), which agrees with similar findings in *Drosophila* immune cells.[12]

Given the observed transcriptional changes in the cellular process of *Pex2*$^{-/-}$ hepatic immune cells, we assessed whether the expression of genes encoding peroxisome-associated proteins was altered in *Pex2*$^{-/-}$ mice. The peroxisomal biosynthetic genes *Pex5*, *Pex6*, *Pex10*, *Pex11b*, *Pex12*, *Pex16*, and *Pex19* exhibited lower expression in B cell lineages (pro-B, large pre-B, and B) and the cDC1 subset of *Pex2*$^{-/-}$ mice compared to WT mice, while, conversely, the expression of these PEXs was higher in nearly every other immune cell type in *Pex2*$^{-/-}$ mice (Figure S2E). The expression of *Pex1*, *Pex3*, *Pex7*, and *Pex13* was lower in these B cell lineages but higher in cDC1 and most other immune subsets in *Pex2*$^{-/-}$ mice. Notably, the expression of *Pex11a* was higher in nearly all hepatic immune subsets of *Pex2*$^{-/-}$ mice, while *Pex11g* was broadly lower.

Altogether, these data confirmed that liver immune cells from a *Pex2*$^{-/-}$ PBD-ZSS mouse model exhibit gene enrichment profiles typical of cells with defects in peroxisomal metabolism.[12,42]

Our analyses also show that genes required for the development and functions of immune cells (e.g., "negative regulation of lymphocyte differentiation," "myeloid cell development") are positively enriched in the *Pex2*$^{-/-}$ versus WT hepatic immune cells as well as immune processes (e.g., phagocytosis, cytokine production involved in immune responses, regulation of myeloid cell activation involved in immune response, and leukocyte degranulation regulation) (Figure S3A). Conversely, negatively enriched processes were identified in categories related to immune functions in the *Pex2*$^{-/-}$ compared to the

Figure 2. Gene expression profiles in *Pex2*$^{-/-}$ compared to WT hepatic immune cells suggest developmental delays

(A) Proportion of cell types identified in scRNA-seq analysis of immune subsets relative to the total number of CD45^{+} cells (top) or relative to the total number of cells of a specific immune subset (bottom).

(B) GSEA of differentially expressed genes between major cell types identified in WT and *Pex2*$^{-/-}$ mice.

(C and D) Relative expression of MHC class II encoding and associated genes across (C) four developing B cell subsets and (D) three dendritic cell (DC) subsets. See Figures S2 and S3 and Tables S3, S4, S5, and S6.

WT hepatic immune environment (e.g., activation of nuclear factor-κB [NF-κB] signaling and presentation of exogenous soluble antigens) (Figure S3B; Table S4). Notably, genes involved in polyamine metabolism are negatively enriched in the *Pex2*$^{-/-}$ hepatic environment; this is important because polyamines have emerged as an important regulator of immune cells' activities, and their metabolism occurs in part in peroxisomes (Figure S3; Table S4).[8] The direct role of peroxisome metabolism in some of the immune functions identified in the GSEA has been demonstrated in *Drosophila* (e.g., phagocytosis and NF-κB signaling)[11] and mouse (e.g., phagocytosis and cytokine production).[12,14] The enrichment of these immune processes in the *Pex2*$^{-/-}$ immune cells supports the idea that the development and function of hepatic immune cells at this stage rely on peroxisomes.

The differential expression profiles of individual *Pex2*$^{-/-}$ liver cells reveal altered states of development and immune processes

To identify changes in cellular processes and programs in major immune subsets present in the *Pex2*$^{-/-}$ neonatal liver, we performed GSEA on the genes with significant differential expression compared to WT mice. We assessed these enrichments across three groups of cells: the GMP and neutrophil group, the myeloid/monocyte group containing GMPs, MDPs, DCs, monocytes, and Kupffer cells, and the group of developing B cells.

Generally, GMPs, as well as all the developing neutrophil subsets of *Pex2*$^{-/-}$ compared to WT, showed a positive enrichment of several lipid metabolic gene sets (e.g., fatty acid catabolism, steroid catabolism, ether lipid metabolism, etc.) and immune pathway gene sets (e.g., NLRP3 inflammasome assembly, regulation of the tumor necrosis factor [TNF] signaling pathway, and antifungal innate immune response). More mNP subsets were positively enriched in gene sets associated with the production of and response to immunoactive molecules (e.g., prostaglandin secretion, eicosanoid metabolism, interleukin-8 [IL-8] production, and complement activation). By contrast, the GMPs, as well as all the developing neutrophil subsets of Pex2$^{-/-}$ compared to WT, collectively showed a negative enrichment in gene sets associated with cell differentiation, calcium release, IL-4 production, antigen presentation, and VLCFA metabolism. The GMPs and more iNP subsets were negatively enriched in genes associated with cell differentiation and cell division, suggesting that granulocyte differentiation programs of the hepatic precursor cells are affected in the severe PBD-ZSS model (Figure 2B; Table S6).

The GSEA patterns within the myeloid/monocyte group of *Pex2*$^{-/-}$ compared to WT show a positive enrichment of gene sets associated with innate immune regulation and Toll-like receptor (TLR) signaling in GMPs, MDPs, all DCs, and Kupffer cells but negatively enriched in monocytes (Figure 2B; Table S6). The MDP, DCs, and Kupffer cells were also positively enriched in gene sets associated with TNF and chemokine production, MAPK and Notch signaling, and cell migration, while GMPs and monocytes were negatively enriched in these processes. cDCs, cDC1s, and cDC2s were negatively enriched in gene sets associated with the actin cytoskeleton, microtubule processes, receptor-mediated endocytosis, and antigen processing and presentation by MHC class II (Figure 2B; Table S6).

The developing subsets of B cells in *Pex2*$^{-/-}$ mice, including pro-B, large pre-B, small pre-B, and B, show an enrichment of upregulated genes associated with plasminogen activation, negative regulation of coagulation, phosphatidylinositol dephosphorylation, and cholesterol efflux (Figure 2B; Table S6). Across the more mature B cell subsets, there is a positive enrichment of the downregulated genes in *Pex2*$^{-/-}$ mice, which are associated with eicosanoid and fatty acid synthesis, leukotriene metabolism, glycerophospholipid catabolism, and IL-12 production. Pro-B cells in *Pex2*$^{-/-}$ mice, by contrast, were enriched in genes upregulated in these processes. Likewise, the immature B cell subsets in *Pex2*$^{-/-}$ mice were enriched with genes associated with immune processes such as antifungal, antimicrobial, and humoral immune responses; IL-1β production; phagosome maturation; and antigen processing and presentation via MHC class II (Figure 2B; Table S6). These processes were negatively enriched in mature B cells, suggesting that mature B cells have defective immune response processes and are deficient in MHC class II antigen presentation. The enrichment of the process of MHC class II antigen processing and presentation among downregulated genes of both the *Pex2*$^{-/-}$ B cells, DC subsets, and neutrophils led us to assess the expression level of specific MHC class II presentation-associated genes in the B and DC subsets. We found that the MHC class II-associated and encoding genes *H2-Aa*, *H2-Ab1*, *H2-Eb1*, *H2-Eb2*, and *Ciita* were downregulated in mature B cells (Figure 2C). Likewise, all DC subsets, cDC1s, cDC2s, and pDCs exhibited a downregulation in most of these genes (Figure 2D).

In conclusion, GSEAs of the differential gene expression between *Pex2*$^{-/-}$ versus WT across all the analyzed immune cell groups suggest lipid metabolic defects, including lipid mediators, cytoskeleton alteration, and deregulation of immune and inflammatory genes, in mature cells. Interestingly, all immune cell precursors show negative enrichments in genes involved in differentiation but a positive enrichment in genes encoding for immune and inflammatory signaling. On the other hand, the enrichment analyses of the downregulated genes in the mutant versus WT mature immune cell populations show defects in immune effector functions (e.g., phagocytosis or antigen presentation). Of interest was the significant downregulation in antigen-presenting genes in mature B cells and DC subsets.

Flow cytometry corroborates developmental defects in myeloid cells and B cells

To validate the scRNA-seq results, we characterized select neonatal liver immune cells of WT and *Pex2*$^{-/-}$ pups by flow cytometry analysis (gating strategy: Figures S4A–S4C). By staining for cell surface markers CD11b, Ly6C, and Ly6G, we identified an increase in the proportion of GMPs (CD11b^{+}Ly6C^{lo}Ly6G^{lo}) and a decrease in the proportion of neutrophils (CD11b^{+}Ly6C^{lo}Ly6G^{hi}) among all viable CD45^{+} liver immune cells of *Pex2*$^{-/-}$ mice compared to WT littermates (Figures 3A–3C). We did not detect a difference in the frequency of monocytes (CD11b^{+}Ly6C^{hi}Ly6G^{lo}) in the *Pex2*$^{-/-}$ liver immune compartment (Figures 3A–3D).

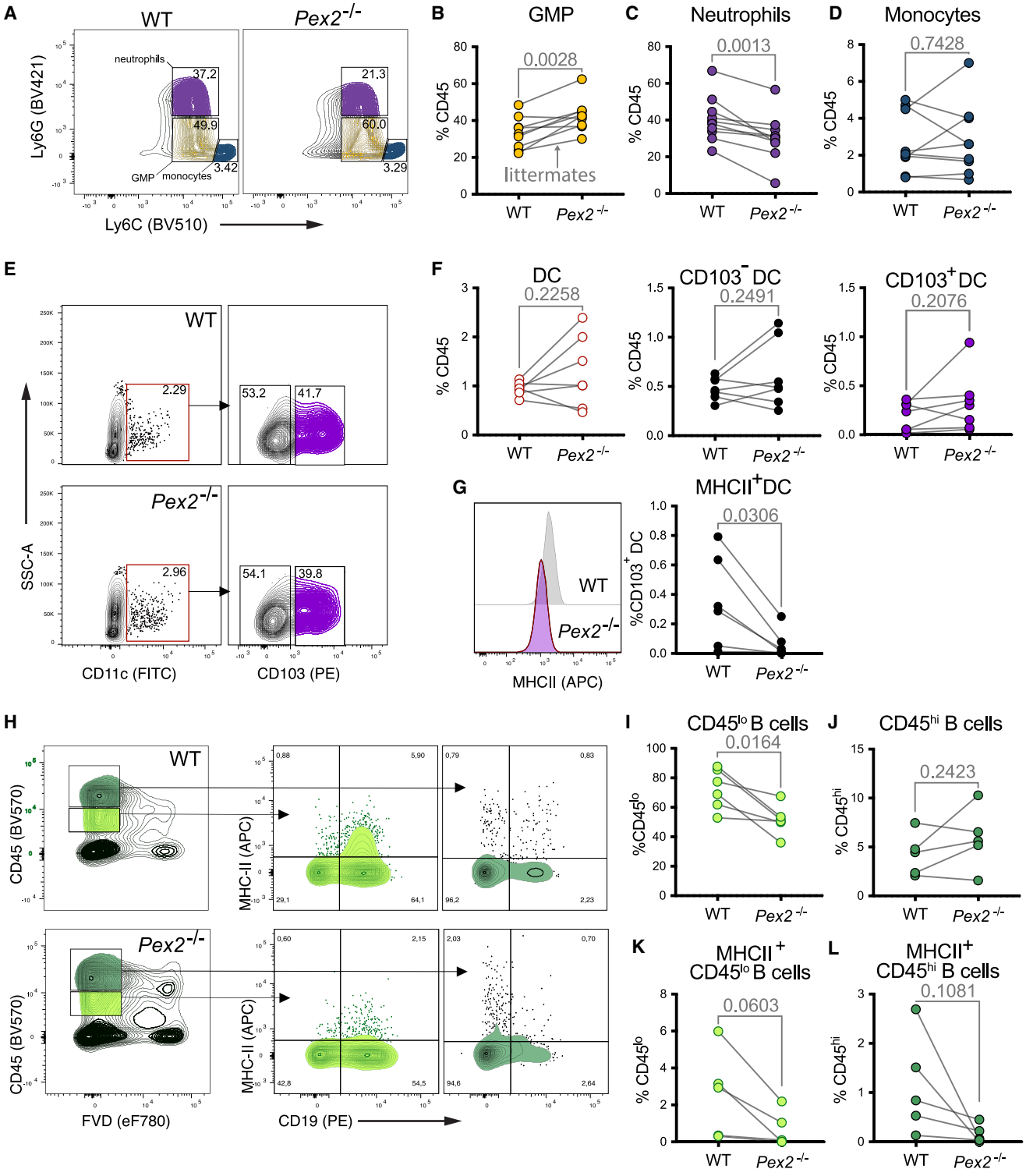

Figure 3. Flow cytometry analyses of hepatic immune populations show developmental defects in hepatic myeloid and lymphoid immune cells

(A) Measurement of hepatic neutrophils (CD11b^{+}Ly6C^{int}Ly6G^{hi}), immature myeloid cells (GMPs) (CD11b^{+}Ly6C^{int}Ly6G^{int}), and classical monocytes (CD11b^{+}Ly6C^{hi}Ly6G^{-}) in livers of WT and *Pex2*$^{-/-}$ mice at neonatal day 0.

(B–D) Quantification of (B) hepatic GMPs, (C) neutrophils, and (D) monocytes in WT and *Pex2*$^{-/-}$ mice.

(E) Identification of hepatic DCs (CD45^{+} CD11c^{+} F4/80^{-} Ly6G^{-}), CD103^{+} DCs, and CD103^{-} DCs in neonatal P0 mouse livers of WT and *Pex2*$^{-/-}$ mice.

(legend continued on next page)

Analysis of the neonatal liver DC population of WT or *Pex2*$^{-/-}$ mice showed similar proportions of total DCs (F4/80^{-} CD11c^{+}) between each genotype, as well as a similar proportion of CD103^{+} and CD103^{-} DC subsets (Figures 3E and 3F). Given the observed downregulation of MHC class II genes in the DC population identified in our scRNA-seq data (Tables S3 and S5), we measured the surface expression of MHC class II in DCs and observed a significantly lower level of MHC class II on the surface of DCs of *Pex2*$^{-/-}$ mice compared to DCs of their WT littermates (Figure 3G).

To examine whether *Pex2*$^{-/-}$ had any detectable differences in the developing hepatic B cell population of postnatal day 0 mice, we stained CD45^{+} liver immune cells for the B cell surface marker CD19. Among liver B cells at postnatal day 0 in either WT or *Pex2*$^{-/-}$ mice, we found that immature B cells (CD45^{lo}CD19^{+}) make up the majority of B cells, while only a few mature B cells (CD45^{hi}CD19^{+}) are detectable at this age (Figure 3H). We detected fewer immature B cells in *Pex2*$^{-/-}$ mice (Figures 3H and 3I) but no change in mature B cells (Figures 3H and 3J). Given the significant changes in DC MHC class II expression, we measured the cell surface expression of MHC class II on either immature or mature B cells. No significant differences in the level of MHC class II on B cells of WT or *Pex2*$^{-/-}$ littermates were detected, although the proportion of MHC class II^{+} B cells trended lower in each replicate (Figures 3K and 3L). Our flow cytometry analysis of the neonatal immune populations of *Pex2*$^{-/-}$ mouse liver reveals a consistent accumulation of immature or progenitor populations for monocytes, neutrophils, and DC lineages, indicating a possible developmental arrest/delay in these cells.

cDCs of *Pex2*$^{-/-}$ mouse display defects in MHC class II expression

The identification of a significant downregulation of genes encoding the MHC class II protein complex in *Pex2*$^{-/-}$ DCs in the scRNA-seq analysis and lower MHC class II surface expression on *Pex2*$^{-/-}$ DCs in the flow cytometry analysis (Figures 2B, 2D, and 3G; Tables S3 and S6) suggested that peroxisome function might affect the antigen-presenting activity of these cells. To identify the functional processes affected in *Pex2*$^{-/-}$ DCs, we performed GSEAs on the differentially expressed genes identified between WT and *Pex2*$^{-/-}$ DCs. Genes with downregulated expression in *Pex2*$^{-/-}$ DCs were enriched in processes associated with antigen processing and presentation, including the MHC class I and II protein complexes, components of the Golgi membrane, the lysosome, and the plasma membrane among gene sets of cellular components queried, while COPI vesicles, which are involved in Golgi-to-endoplasmic reticulum retrograde trafficking of MHC protein complexes, were associated with genes with upregulated expression in *Pex2*$^{-/-}$ DCs (Figure 4A). Among biological processes queried, we found that genes with downregulated expression in *Pex2*$^{-/-}$ DCs were associated with myeloid leukocyte differentiation, long-chain fatty acid metabolism, and inflammatory responses to antigenic stimulus (Figure 4B). Conversely, we identified an enrichment of genes with upregulated expression in *Pex2*$^{-/-}$ DCs associated with negative regulators of lipid metabolism and glycerolipid catabolism (Figure 4B). Given these observations and the data reported above, we decided to investigate the antigen presentation activities in cDCs further.

As the population of cDCs in a liver at day 0 is very small, it would have been complex and ethically challenging to dissect the antigen presentation signaling in hepatic *Pex2*$^{-/-}$ compared to that in WT cDCs. We planned to isolate CD45^{+} circulating immune cells in peripheral blood to probe the hematopoiesis efficiency of liver and bone marrow-derived cDCs from day 0 mice and study the peroxisome requirement in antigen presentation. However, the extraction of immune cells from the peripheral blood of the *Pex2*$^{-/-}$ mouse on day 0 yielded a meager cell count incompatible with the experimental requirements (Figure S4D). Furthermore, due to the high penetrance and expressivity of the lethality phenotype in the murine *Pex2*$^{-/-}$ PBD-ZSS model, we could not conduct the analyses on peripheral blood at a later age to obtain more cells from the blood. For these reasons, we studied the antigen presentation requirements for peroxisomes using bone marrow-derived DCs (BMDCs) from *Pex2*$^{-/-}$ and WT day 0 mice *in cellulo*.

Flow cytometry analyses confirmed that *in-vitro*-differentiated BMDCs express the canonic markers for cDCs (Figure 4C). To assess antigen presentation upon immune activation in *Pex2*$^{-/-}$ BMDCs, we measured the surface expression of CD8a, CD11c, the co-stimulatory molecules ICAM1 and CD80, and the class I and II MHC protein complexes in WT and *Pex2*$^{-/-}$ BMDCs at baseline and upon stimulation with lipopolysaccharides (LPSs). We did not detect surface expression of CD8a on WT or *Pex2*$^{-/-}$ BMDCs under any condition. The differentiation marker CD11c was highly expressed on BMDCs from WT and *Pex2*$^{-/-}$ and did not change with LPS treatment (Figure 4C). We observed an upregulation of the co-stimulatory markers ICAM1 and CD80 in LPS-stimulated *Pex2*$^{-/-}$ BMDCs versus WT cells; however, we found that the surface expression of MHC class I and II protein complexes was significantly lower in *Pex2*$^{-/-}$ BMDCs in both unstimulated and LPS-stimulated conditions (Figure 4C). Since the flow cytometry analyses carried out in BMDCs corroborate the results of the scRNA-seq, which showed a low expression of MHC class II genes in hepatic DCs of *Pex2*$^{-/-}$ mice, we performed reverse-transcription quantitative polymerase chain reaction (RT-qPCR) experiments to measure the expression of the genes encoding the class II MHC protein complex, *H2-Aa*, *H2-Ab*, and *H2-DMb*. We recorded lower expression for *H2-Aa*, *H2-Ab*, and *H2-DMb* transcripts in *Pex2*$^{-/-}$ compared to WT BMDCs (Figures 4D–4F), as observed in the hepatic cDCs (Table S5). Upon LPS stimulation, the H2-Aa, H2-Ab, and

(F) Quantification of hepatic DC subsets.
(G) Measurement and quantification of surface MHC class II expression on CD103^{+} DCs.
(H) Identification of mature B cells (CD45^{hi} CD19^{+}) and immature B cells (CD45^{lo} CD19^{+}) in P0 neonatal mouse livers of WT and *Pex2*$^{-/-}$ mice.
(I–L) Quantification of (I) immature and (J) mature B cells and (K and L) their respective surface expression of MHC class II. A connecting line indicates littermates. Significance determined by paired t test with p values for each comparison are shown. n = 5–8 independent experiments.
See Figure S4.

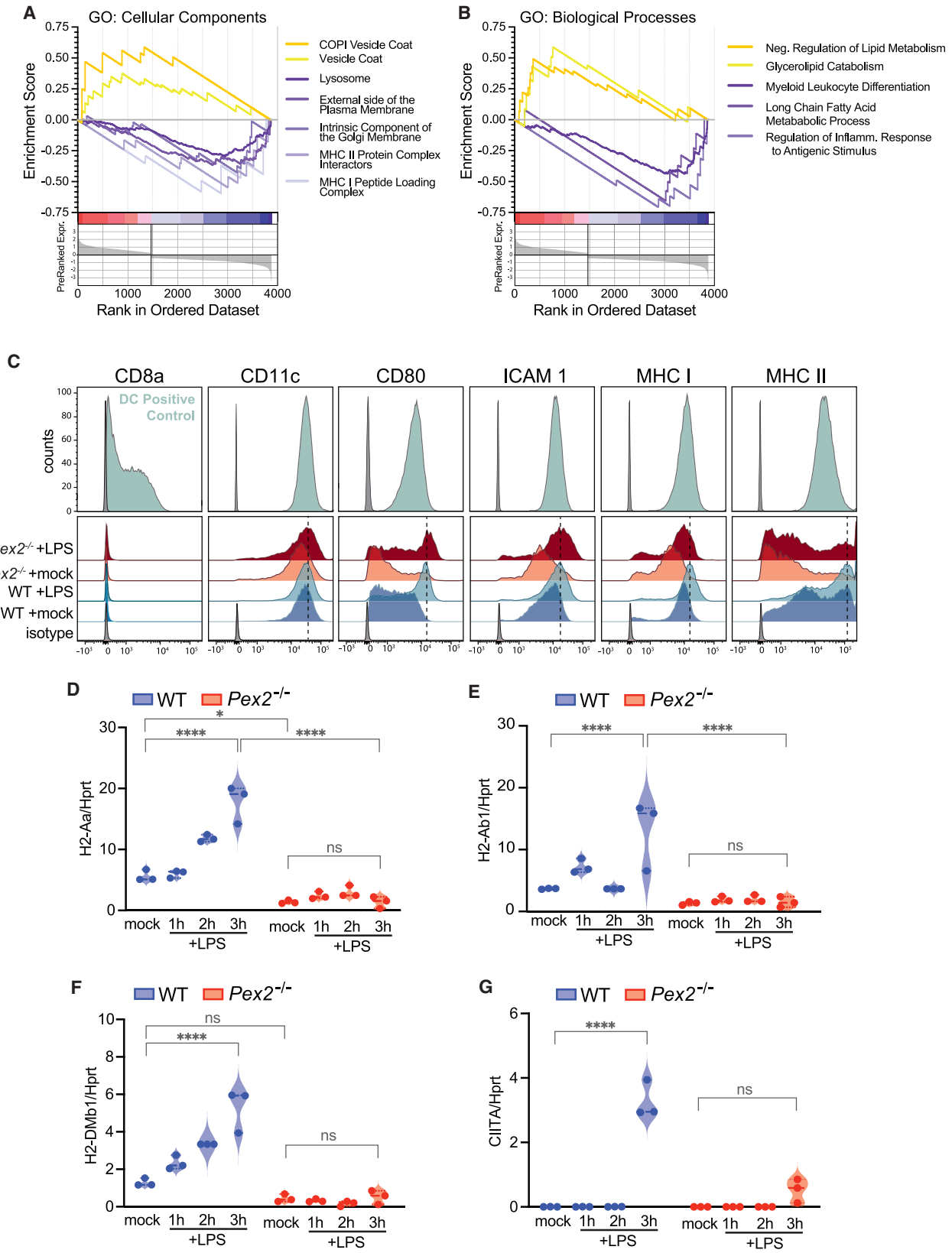

(legend on next page)

H2-DMb transcripts were remarkably upregulated over 3 h of treatment. However, no significant induction was observed in stimulated *Pex2*$^{-/-}$ BMDCs (Figures 4D–4F). *H2-Aa*, *H2-Ab*, and *H2-DMb* are transcribed by the transcription factor MHC class II transactivator (CIITA)[43]; we found that the CIITA transcript is downregulated in *Pex2*$^{-/-}$ versus WT BMDCs in both unstimulated and LPS-stimulated cells (Figure 4G). These results demonstrate that BMDCs from *Pex2*$^{-/-}$ murine model mice can differentiate into mature cDCs expressing canonical markers of differentiation. However, as observed in the hepatic cDCs, these cells exhibit deregulation of MHC class II genes, suggesting that this is not caused by developmental and growth delays of *Pex2*$^{-/-}$ animals. Of note, the upregulation of co-stimulatory factors was observed in the CIITA mutant murine model,[43] indicating that the upregulation of co-stimulatory factors might be a compensatory mechanism.

PKC activity is low in BMDCs of *Pex2*$^{-/-}$ mice

Peroxisome lipid metabolism has been described as a modulator of differentiation and/or activation signaling in iNKT cells,[44] macrophages,[11,12,14] mast cells,[15] T cells, and B cells.[16] CIITA is regulated at the transcriptional and posttranscriptional levels by activating Protein kinase C delat (PKC-δ).[45–47] PKC isoforms comprise a family of lipid-activated enzymes, and PKC-δ is one of the PKC isoforms highly expressed in DCs and specifically involved in the regulation of MHC class II expression.[47] We measured the activity of PKC-δ in WT and *Pex2*$^{-/-}$ BMDCs under unstimulated conditions and upon stimulation with LPS. PKC activity increased in WT BMDCs after 3 h of stimulation but not in *Pex2*$^{-/-}$ BMDCs (Figure 5A). PKC-δ is denoted as a novel PKC isoform[48] and is activated exclusively by membrane-bound diacylglycerols (DAGs) or phorbol 12-myristate 13-acetate (PMA), both of which anchor PKCs in their active conformations to membranes.[49] We measured PKC-δ activity in WT and *Pex2*$^{-/-}$ BMDCs treated with PMA, which mimics DAGs, and observed that PMA alone is sufficient to promote strong activation of PKC-δ. Our results show that PKC activity increases in both WT and *Pex2*$^{-/-}$ BMDCs treated with both PMA and LPS (Figure 5A), suggesting that peroxisomes control PKC activity in LPS-stimulated BMDCs. In previous work, we showed that peroxisome-depleted macrophages accumulate DAG species mainly with unsaturated VLCFAs ($\geq$C22) while exhibiting reduction of DAG with saturated and unsaturated long-chain fatty acids, and these differences were enhanced during the immune challenge.[12] Moreover, our functional annotation of differentially regulated genes in pseudo-bulk analyses from the scRNA-seq showed that genes belonging to glycerolipid (e.g., DAG) metabolic processes were differentially enriched in *Pex2*$^{-/-}$ versus WT liver immune cells. We assessed the expression of enzymes involved in DAG metabolism and observed that genes required for DAG synthesis such as *Lpin1*, *Lpin2*, and *Pnpla2*, which produce DAGs from phosphatidic acids (PAs) and triacylglycerides, respectively, were downregulated in cDC1 *Pex2*$^{-/-}$ versus WT (Figure S2E). On the other hand, genes that encode DAG kinases and CDP-choline diacylglycerol choline phosphotransferases that can transform DAGs into PAs and phosphatidylcholines, respectively, were downregulated or unchanged in *Pex2*$^{-/-}$ versus WT (Figure S2E). These transcriptional analyses suggest that DAG metabolism might be altered in *Pex2*$^{-/-}$ versus WT cDC1s. Thus, we measured the cellular concentration of DAGs in WT and *Pex2*$^{-/-}$ in mock- or LPS-treated BMDCs. *Pex2*$^{-/-}$ BMDCs have lower DAG concentrations in mock-treated and LPS-treated conditions (Figure 5B). Considering that PKC-δ is the major DAG inducible isoform in murine DCs,[47] our data suggest that *Pex2*$^{-/-}$ BMDCs do not have the required amount/species of DAGs upon LPS stimulation necessary to trigger PKC-δ-mediated signaling.

PKC-δ activation is required to restore MHC class II expression in *Pex2*$^{-/-}$ BMDCs

To further establish a requirement for PKC-δ activation in DCs upon LPS stimulation, we measured the activation of PKC-δ by both indirect immunofluorescence and western blotting experiments. The activation of PKC-δ is controlled by DAG-mediated recruitment of the kinase to the plasma membrane followed by autophosphorylation of serine 643 of PKC-δ.[50] We used an antibody specific to the phosphorylated serine 643 residue of PKC-δ to measure the amount of phosphorylated PKC-δ (P-PKC-δ) in WT and *Pex2*$^{-/-}$ BMDCs by indirect immunofluorescence. Our data showed a higher cellular amount of P-PKC-δ in LPS-stimulated and unstimulated WT BMDCs compared to *Pex2*$^{-/-}$ BMDCs (Figures 5C and 5D). We treated WT and *Pex2*$^{-/-}$ BMDCs with PMA and observed that both WT BMDCs and *Pex2*$^{-/-}$ BMDCs showed an elevated cellular amount of P-PKC-δ (Figures 5C and 5D). We confirmed these results by western blot, which showed that P-PKC-δ increases in WT BMDCs upon 3 h of LPS stimulation or treatment with PMA followed by LPS stimulation (Figures 5E and 5F). In *Pex2*$^{-/-}$ BMDCs, P-PKC-δ levels did not increase after 3 h of LPS stimulation but dramatically increased upon treatment with PMA followed by LPS stimulation (Figures 5E and 5F). Measurement of PKC-δ and α-tubulin protein levels as loading controls showed that the amounts of these proteins did not change upon any treatment of WT BMDCs, while the amount of PKC-δ in *Pex2*$^{-/-}$ BMDCs treated with PMA and LPS was lower (Figures 5E–5G). Despite this decrease in

Figure 4. *Pex2* is required for the induction of MHC class II genes

(A and B) Select GSEA of differentially expressed genes in *Pex2*$^{-/-}$ versus WT hepatic DCs that were significantly enriched in functional categories of (A) cellular components and (B) biological processes that impact the core activity of DCs.

(C) Flow cytometry analyses measuring cDC differentiation markers on a positive control cDC line versus isotype controls (top) on *in-vitro*-differentiated WT and *Pex2*$^{-/-}$ BMDCs in response to mock treatment or LPS treatment (bottom).

(D–G) Violin and dot plots showing RT-qPCR measurements of (D) H2-Aa, (E) H2-Ab, (F) H2-DMb1, and (G) CIITA transcript relative expression versus the internal control transcript Hprt in mock-treated and LPS-treated BMDCs over time.

n = 3 independent experiments. Statistical significance was calculated by two-way ANOVA test, ****p < 0.0001,***p < 0.001, *p < 0.05, ns not significant.
See Figures S2 and S3 and Tables S3, S4, S5, and S6.

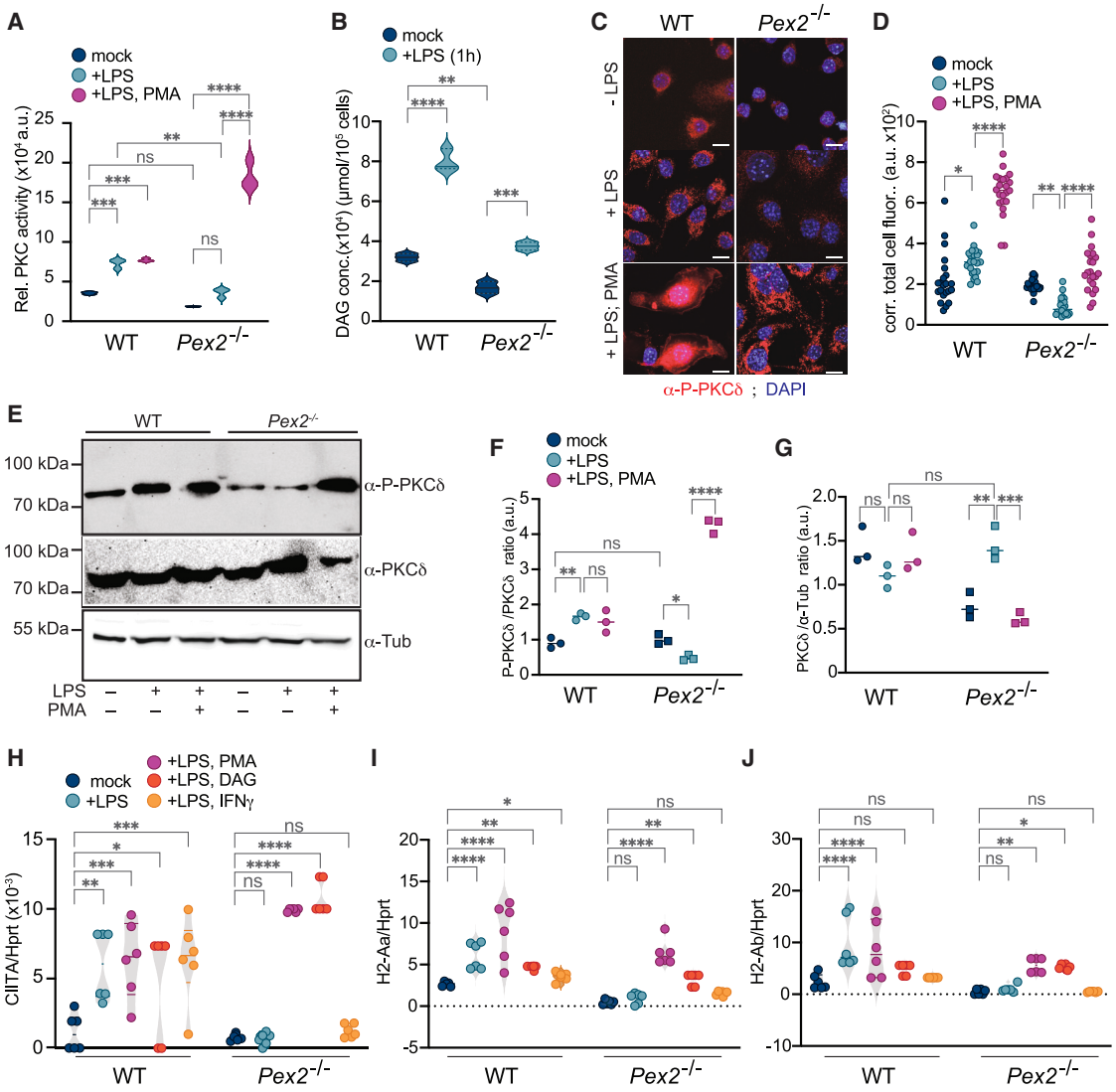

Figure 5. *Pex2* regulates DAG-PKC-δ signaling to activate CIITA and MHC class II in BMDCs

(A) Violin plots showing relative PKC activity in the BMDCs of the reported genotypes and under the indicated treatments.

(B) Violin plots showing concentrations of DAG in BMDCs of the reported genotypes.

(C) Indirect immunofluorescence indicating P-PKC-δ in WT and *Pex2*$^{-/-}$ BMDCs treated with vehicle, LPS, or PMA plus LPS. Scale bar: 10 μm.

(D) Dot plot quantification of P-PKC-δ in the indirect immunofluorescence experiments represented in (C). n = 20 cells.

(E) Representative western blot image to detect P-PKC-δ and PKC-δ in WT and *Pex2*$^{-/-}$ BMDCs treated with vehicle, LPS, or PMA plus LPS. α-Tubulin is used as a loading control.

(F) The bar graph represents ratiometric analyses of the mean intensity value between P-PKC-δ and PKC-δ in western blot experiments. n = 3 independent experiments.

(G) The bar graph represents ratiometric analyses of the mean intensity value between PKC-δ and α-tubulin in western blot experiments. n = 3 independent experiments.

(H–J) Dot and violin plots representing the expression of (H) CIITA, (I) H2-Aa, and (J) H2-Ab transcripts relative to the expression of Hprt transcript used as an internal control in WT and *Pex2*$^{-/-}$ BMDCs treated with vehicle, LPS, PMA plus LPS, DAG plus LPS, or IFNγ plus LPS.

n = 3 in (A), (B), (F), and (G) and 6 independent experiments in (H)–(J). Statistical significance was calculated by two-way ANOVA test, ****p < 0.0001, ***p < 0.001,**p < 0.01, *p < 0.05, ns not significant.

PKC-δ in *Pex2*$^{-/-}$ BMDCs, these cells are able to achieve similar levels of PKC-δ phosphorylation to WT in BMDCs in response to PMA, indicating that PMA is sufficient to activate PKC-δ to levels detected in WT and rescue DC responsiveness to LPS.

Since PKC-δ activation can regulate the expression of CIITA and MHC class II genes,[45–47] we tested whether CIITA and MHC class II gene expression is modulated by the activation of PKC-δ induced by PMA or by the DAG analog 1,2-dioctanoyl-*sn*-glycerol, a 1,2-diacyl-*sn*-glycerol, where both the 1- and

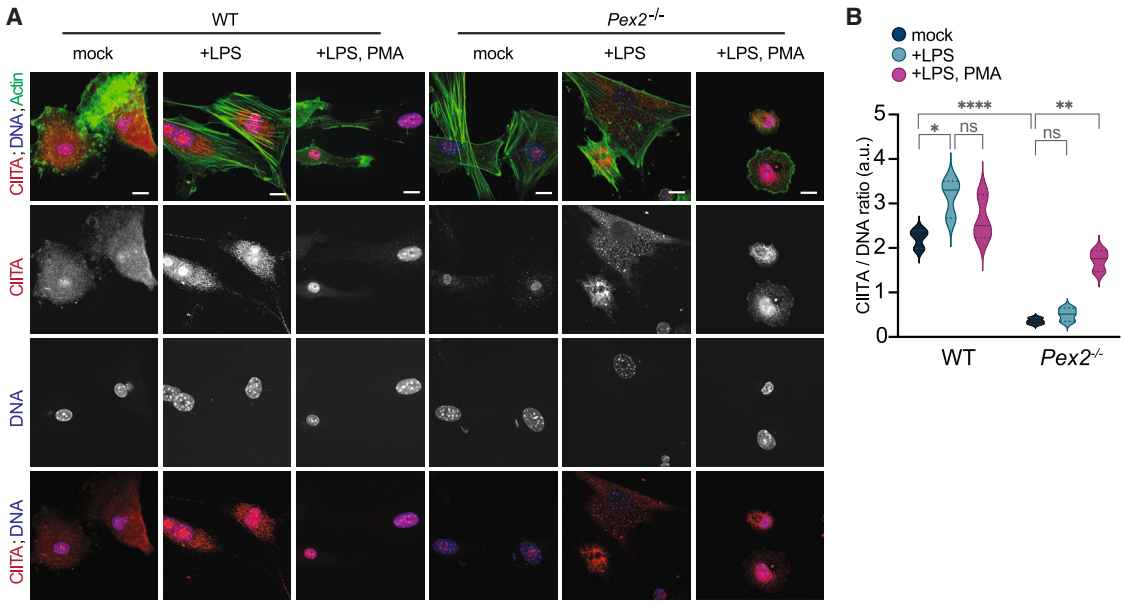

Figure 6. *Pex2* regulates CIITA cellular amount and localization

(A) Indirect immunofluorescence indicating CIITA in WT and *Pex2*$^{-/-}$ BMDCs treated with vehicle, LPS, or PMA plus LPS. Scale bar: 10 μm.

(B) Dot plot quantification of CIITA/DAPI ratiometric fluorescence intensity values in the indirect immunofluorescence experiments represented in (A). n = 20 cells. Statistical significance was calculated by two-way ANOVA test, ****p < 0.0001, **p < 0.01, *p < 0.05, ns not significant.

2-acyl groups are specified as octanoyl fatty acid chains, which are endpoints of β-oxidation in peroxisomes.[51] This DAG is a cell-permeable analog of the PKC-activating second-messenger DAG.[52,53] DAG treatment of *Pex2*$^{-/-}$ BMDCs rescues *Ciita*, *H2-Aa*, and *H2-Ab* transcription (Figures 5H–5J). We observed upregulation of the CIITA transcript in WT BMDCs treated with either LPS, LPS plus PMA, or LPS plus DAG compared to mock-treated BMDCs (Figure 5H). On the other hand, CIITA transcript levels were not induced in *Pex2*$^{-/-}$ BMDCs upon LPS stimulation but were upregulated upon treatment with LPS and PMA and with LPS and DAG, suggesting that activation of PKC-δ is required for the transcriptional induction of *Ciita* (Figure 5H). We then measured *H2-Aa* and *H2-Ab* induction in WT and *Pex2*$^{-/-}$ BMDCs during stimulation with LPS, LPS plus PMA, or LPS plus DAG. Our RT-qPCR results indicate that *H2-Aa* transcription is enhanced in WT cells upon each stimulation, while only LPS plus PMA and LPS plus DAG treatments were sufficient to induce *H2-Aa* transcription in *Pex2*$^{-/-}$ BMDCs (Figure 5I). LPS treatment alone did not induce *H2-Aa* expression in *Pex2*$^{-/-}$ BMDCs (Figure 5I). Measurement of *H2-Ab* transcription showed an increase in WT BMDCs upon LPS or LPS plus PMA (Figure 5J); however, as with *Ciita* and *H2-Aa*, the expression of *H2-Ab* was not induced in LPS-treated *Pex2*$^{-/-}$ BMDCs, but treatment with the PKC-δ activator PMA or DAG rescued the LPS-stimulated *H2-Ab* induction in the mutant BMDCs (Figure 5J).

Interferon-γ (IFNγ) can induce *Ciita* gene expression and, therefore, MHC class II encoding genes in macrophages, DCs, and B cells.[45,54–56] PKC-δ is crucial in regulating IFNγ-mediated regulation of *CIITA* gene expression.[45] We measured the transcriptional expression of *Ciita*, *H2-Aa*, and *H2-Ab* in WT and *Pex2*$^{-/-}$ BMDCs after 12 h of treatment with IFNγ. Using RT-qPCR analyses, we detected the induction of *Ciita* and *H2-Aa* in WT BMDCs after IFNγ treatment (Figures 5H–5J). *Ciita* and *H2-Aa* were not transcriptionally induced in IFNγ-treated *Pex2*$^{-/-}$ BMDCs (Figures 5H–5J). However, we could not detect the induction of *H2-Ab* either in WT or *Pex2*$^{-/-}$ BMDCs in our experimental conditions. These data suggested that IFNγ-mediated induction of *Ciita* and *H2-Aa* requires functional peroxisomes.

We confirmed the requirement of peroxisome metabolism for CIITA expression at protein levels by performing indirect immunofluorescence and western blot experiments using an anti-CIITA antibody. Indirect immunofluorescence experiments showed that CIITA increases in both the cytoplasm and nucleus of BMDCs after a 3 h stimulation with LPS. It is exclusively nuclear in BMDCs pre-treated with PMA and then stimulated with LPS (Figures 6A and 6B). In *Pex2*$^{-/-}$ BMDCs, CIITA was less detectable in both the cytoplasm and nucleus but was present in the nuclei of *Pex2*$^{-/-}$ BMDCs pre-treated with PMA and stimulated for 3 h with LPS, confirming that PMA can trigger the expression/stability of CIITA (Figure 6A). Western blot analyses confirmed that CIITA is less in *Pex2*$^{-/-}$ BMDCs than in WT BMDCs (Figures 7A and 7B), but PMA increased the cellular amount of CIITA to the levels present in WT BMDCs (Figures 7A and 7B). We concluded that peroxisomes are required for the PKC-δ-mediated induction of *Ciita* and of *H2-Aa* and *H2-Ab* in BMDCs, in unstimulated conditions, and upon stimulation with LPS or IFNγ.

Peroxisomes regulate MHC class II expression and antigen presentation to T cells

Flow cytometry experiments indicate that surface MHC class II is lower in differentiated *Pex2*$^{-/-}$ BMDCs than in WT

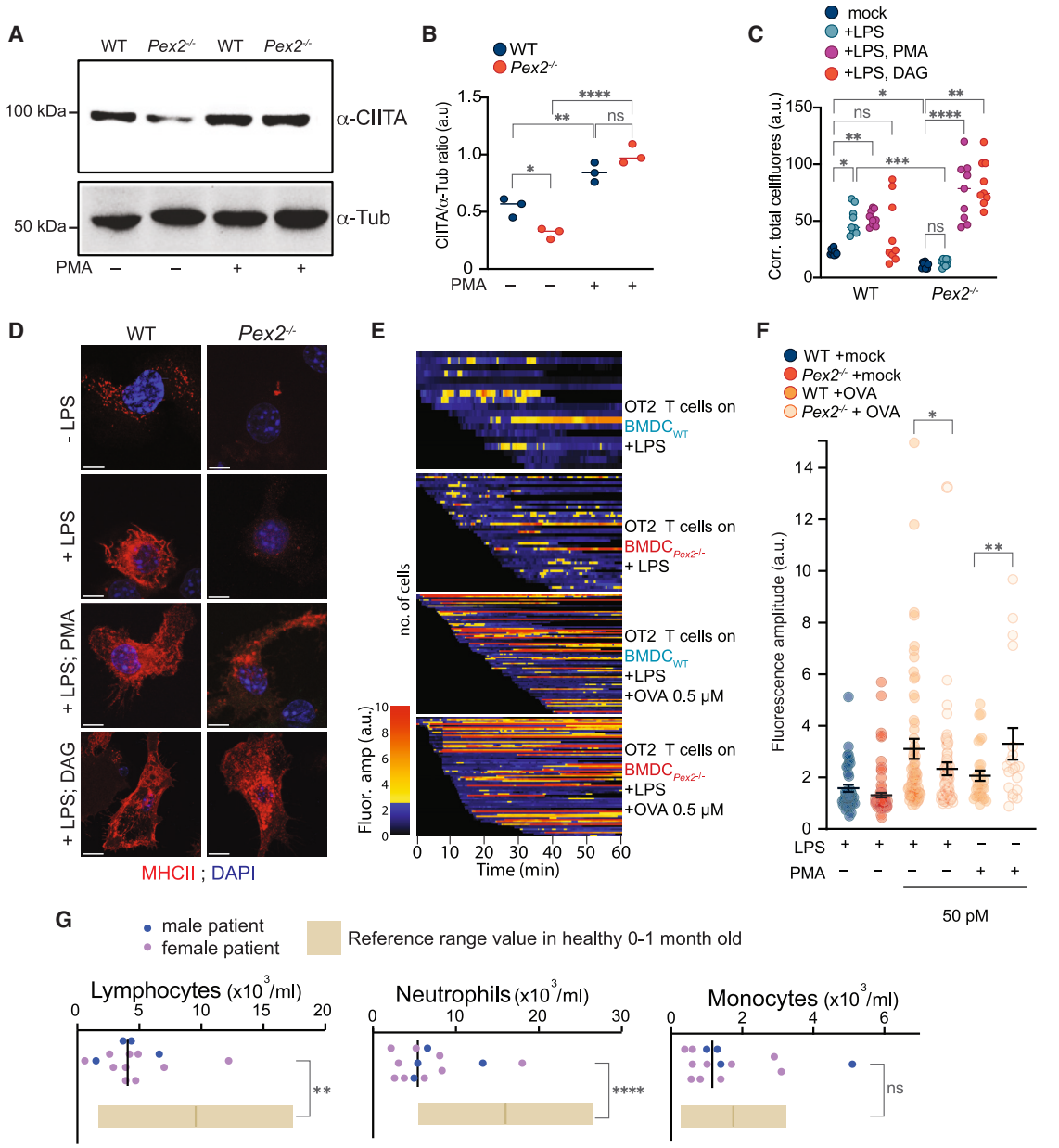

Figure 7. Activation of PKC-δ in WT and *Pex2*$^{-/-}$ BMDCs rescues MHC class II exposure and antigen presentation to CD4^{+} T cells

(A) Representative western blot image to detect CIITA in WT and *Pex2*$^{-/-}$ BMDCs treated with vehicle or PMA. α-Tubulin is used as a loading control.

(B) The bar graph represents ratiometric analyses of the mean intensity value between CIITA and α-tubulin in western blot experiments. n = 3 independent experiments.

(C) Dot plot quantification of MHC class II in the indirect immunofluorescence experiments represented in (D). n = 10 cells.

(D) Representative indirect immunofluorescence images indicating MHC class II in WT and *Pex2*$^{-/-}$ BMDCs treated with vehicle, LPS, LPS plus PMA, or LPS plus DAG. Scale bar: 10 μm.

(E) The diagrams represented cytosolic calcium fluxes in time-lapse movies.

(F) Dot plot quantification of the fluorescence amplitude of the calcium fluxes recorded in CD4^{+} T cells co-cultured with WT and *Pex2*$^{-/-}$ incubated with OVA and stimulated with LPS or PMA plus LPS. n= 25 cells.

(G) Dot plots of total cell count of lymphocytes, neutrophils, and monocytes in the peripheral blood. n = 14.

Statistical significance in (A)–(C) and (F) was calculated by two-way ANOVA test, and statistical significance in (G) was calculated by unpaired t test, ****p < 0.0001, ***p < 0.001, **p < 0.01, *p < 0.05, ns not significant.

BMDCs (Figures 3, 4C, and S5A). However, PMA treatments remarkably enhanced the MHC class II surface signal in WT and *Pex2*$^{-/-}$ BMDCs (Figure S5A). We performed indirect immunofluorescence using the same antibody and observed high MHC class II in WT BMDCs unstimulated and stimulated with LPS for 3 h. Conversely, the MHC class II signal was very low or absent from the cell surface in *Pex2*$^{-/-}$ BMDCs in both unstimulated and stimulated conditions (Figures 7C and 7D). Treatment with PMA or DAG followed by stimulation with LPS rescued MHC class II expression and surface exposure in *Pex2*$^{-/-}$ BMDCs to WT levels and higher (Figures 7C, 7D, and S5A). The inability to expose MHC class II can impact the efficiency of antigen presentation to activate T cells. Therefore, we performed a calcium antigen presentation assay to probe antigen presentation in WT and *Pex2*$^{-/-}$ BMDCs.[57]

Differentiated BMDCs from both genotypes were stimulated overnight with or without LPS and then incubated for 3 h with 0.5 mM chicken ovalbumin (OVA) 323-339 peptide that binds to the I-A MHC class II in the presence of LPS and PMA. Under each condition, WT and *Pex2*$^{-/-}$ BMDCs were washed and incubated with CD4$^+$ T cells isolated from transgenic mice expressing the OVA-specific I-A^b-restricted TCR (OT-II). We performed calcium imaging of OT-II CD4$^+$ T cells in co-culture and monitored antigen-specific calcium signaling as an indication of T cell activation. We found that OT-II CD4$^+$ released more intense calcium signaling when incubated with WT BMDCs stimulated with LPS compared to unstimulated WT BMDCs or to unstimulated and stimulated *Pex2*$^{-/-}$ BMDCs (Figures 7E and 7F). *Pex2*$^{-/-}$ BMDCs stimulated with LPS can trigger a modest calcium signaling in OT-II CD4$^+$ T cells (Figures 7E and 7F), but it is significantly lower than what we observed in stimulated WT BMDCs, suggesting that *Pex2*$^{-/-}$ BMDCs had reduced antigen presentation activity (Figures 7E and 7F). PMA treatment of *Pex2*$^{-/-}$ BMDCs fully rescued the antigen presentation activity to OT-II CD4$^+$ T cells of *Pex2*$^{-/-}$ BMDCs (Figures 7E and 7F). In parallel, we analyzed the expression level of the DC differentiation marker CD11c by flow cytometry, and we observed that differentiation was not affected by PMA treatments in both WT and *Pex2*$^{-/-}$ BMDCs (Figure S5A). We therefore concluded that peroxisomes are required to modulate DAG signaling at the plasma membrane and to activate pathways that promote antigen uptake, exposure of MHC class II, and antigen presentation activity to CD4$^+$ T cells in DCs. Differentiation of cDCs in the hepatic environment of *Pex2*$^{-/-}$ mice is compromised or delayed. Interestingly, BMDCs from *Pex2*$^{-/-}$ mice can differentiate *in vitro* to mature DCs, but the MHC class II expression is lower in *Pex2*$^{-/-}$ BMDCs than in WT cells, as observed in *Pex2*$^{-/-}$ hepatic cDCs. The MHC class II expression can be rescued by pharmacological activation of PKC-δ, which is sufficient to restore the antigen presentation activity of *Pex2*$^{-/-}$ BMDC to CD4$^+$ DCs.

Antigen presentation activity to CD4$^+$ T cells is not affected in *Pex2*$^{-/-}$ macrophages

To understand if peroxisome function is a general requirement for antigen presentation activity, we tested if other antigen-presenting cells in *Pex2*$^{-/-}$ mice exhibited similar defects in antigen presentation. We assessed antigen presentation by BMDMs from *Pex2*$^{-/-}$ mice alongside BMDCs. We performed calcium imaging upon co-culture with OT-II CD4$^+$ T cells and monitored antigen-specific calcium signaling to indicate T cell activation. We found that OT-II CD4$^+$ T cells released more intense calcium signaling when incubated with WT BMDCs compared to *Pex2*$^{-/-}$ BMDCs regardless of prior LPS stimulation (Figures S5B). We could also detect calcium signaling when OT-II CD4$^+$ T cells were incubated with WT or *Pex2*$^{-/-}$ BMDMs; however, we did not record significant differences when OT-II CD4$^+$ T cells were incubated with WT or *Pex2*$^{-/-}$ BMDMs, suggesting that peroxisome function is not required for macrophage antigen presentation (Figure S5B).

We performed RT-qPCR to measure CIITA and H2-Aa transcripts. CIITA and H2-Aa transcripts were significantly lower in *Pex2*$^{-/-}$ BMDMs than in WT when cells were not stimulated with LPS (Figures S5C and S5D). When BMDMs were stimulated for 3 h with LPS, we did not record differences in the CIITA transcript level (Figure S5C). The H2-Aa transcript was lower in *Pex2*$^{-/-}$ BMDMs relative to stimulated WT BMDMs (Figure S5D); however, the difference was not as striking as the one observed between WT and *Pex2*$^{-/-}$ BMDCs. We concluded that *Pex2* is partially required to express MHC class II encoding gene *H2A-a* in BMDMs.

To determine if the observed decrease in antigen presentation was in part a result of reduced antigen uptake, we also tested the uptake rate of OVA-Alexa Fluor 488 in WT and *Pex2*$^{-/-}$ BMDCs and observed a very small but significant reduction in the uptake of OVA-Alexa Fluor 488 in *Pex2*$^{-/-}$ BMDCs relative to WT BMDCs, suggesting that *Pex2*$^{-/-}$ BMDCs have reduced phagocytosis (Figures S5E and S5F), an immune defect observed in macrophages with a deficiency in peroxisome biogenesis,[11,12] but not to the extent that they deplete MHC class II exposure upon stimulation.

Hematopoietic defects are detected in the *Pex2*$^{-/-}$ murine spleen and in the peripheral blood of patients with PBD-ZSS

We probed whether hematopoietic defects in *Pex2*$^{-/-}$ mice were detectable outside the liver. We probed the immune landscape of neonatal spleen from WT and *Pex2*$^{-/-}$ mice. We performed flow cytometry analyses on CD45$^+$ cells and isolated neutrophils (Lys6G), red pulp macrophages (F4/80), and B cells (CD19). We found that *Pex2*$^{-/-}$ mice have fewer total splenic immune cells than WT mice (Figure S5G). Furthermore, when we selected specific myeloid and lymphoid populations, we found that red pulp macrophages (F4/80$^+$), neutrophils (Ly6g$^+$), and B cells (CD19$^+$) were reduced in *Pex2*$^{-/-}$ spleen compared to the WT spleen (Figures S5H–S5J). These data suggested that hematopoietic defects are also detected in other tissues of the *Pex2*$^{-/-}$ mouse.

We then enquired whether children affected by PBD-ZSS show a reduction in white blood cells at birth. We analyzed peripheral blood mononuclear cells of thirteen patients affected by PBD-ZSS, each carrying defined mutations in different PEX genes (six patients with mutation in *Pex1*, one patient in *Pex26*, one in *Pex5*, four in *Pex6*, and one in *Pex10*) and one undefined. All patients were between 0 and 1 month old (human age corresponding to day 0 in mice) and were tested one or more times. Therefore, we averaged the results obtained from the count of the immune cells of each blood withdrawal. We observed that

neutrophil and lymphocyte numbers were significantly low and ranked close to the minimum value reported in healthy children in the same age range (Figure 7G) for each cell type. The number of monocytes in the patients was comparable to the low content value reported in healthy children in the same age range. However, the reduction was not statistically significant (Figure 7G). This preliminary study in PBD-ZSS suggests that hematopoiesis might be affected in patients with PBD-ZSS, at least in the first months of life.

DISCUSSION

We defined the requirement for peroxisomes in developmental hematopoiesis, demonstrating that severe PBD-ZSS presents hematopoietic alteration in the neonatal liver.

The connection between peroxisome dysfunction and impaired cellular development and survival is known.[4,58] Our characterization of the hepatic immune landscape of the PBD-ZSS *Pex2*$^{-/-}$ mouse model suggests that the metabolic dysfunctions that arise due to failed peroxisomal biogenesis prompt differentiation defects in the immune system of children with PBD-ZSS. In the past 30 years, few clinical cases have described immune defects in specific immune cells in young patients with PBD-ZSS that did not carry a mutation in genes linked to immunodeficiences.[5,6,59] Our study provides evidence that peroxisomes are required to develop the immune system, and in this view, the link between primary immunodeficiencies and metabolic disorders should not be undervalued. Indeed, as highlighted in a recent paper,[7] many other metabolic diseases are known to cause immunological defects: adenosine-deaminase deficiency leads to severe combined immunodeficiencies,[60] and familial hemophagocytic lymphohistiocytosis is caused by alterations in the molecular mechanisms involved in vesicle transport and membrane trafficking processes.[61] Additionally, in the past 10 years, multiple studies reported that the peroxisome or its metabolites control various immune cell functions and signaling in response to microbial challenges, such as phagocytosis, TLR-mediated cytokine secretions,[12,15] MAVS activation,[13] NF-κB activity, and RhoGTPase signaling.[11,12] Alteration of these signaling processes has been linked to the development of immune disorders.[62–65] Considering all the above, and since the characterization of peroxisome diseases is incomplete, we firmly believe that immune phenotyping should be performed for all patients with suspected or proven peroxisome disorders to identify strategies to ameliorate the status of PBD-ZSS. A case study reporting the use of allogeneic hematopoietic stem cell transplantation (allo-HSCT) to treat PEX1− PBD-ZSS found that allo-HSCT was effective at lowering the VLCFA level in serum and alleviating disease symptoms in the patient during the short-term follow-up.[66] Allo-HSCT has also been used to treat X-linked adrenoleukodystrophy (X-ALD). It has been shown to have good long-term efficacy at improving survival rates in patients if applied in the early stage of the disease. The long-term benefits of allo-HSCT in X-ALD are thought to be mediated by donor-derived replacement of myeloid-derived cells,[67] supporting the importance of detecting and addressing immune defects in PBD-ZSS.

The liver at postnatal day 0 is a reservoir of cells at different stages of development and pluripotency. This aligns with evidence that the liver remains a central organ for immune cell maturation after birth in rodents,[19] as other sites of immune cell development are aplastic during the first week of life, and that the neonatal immune system may rely on alternative organs to finalize maturation. The liver environment receives primary antigen inputs from the gastrointestinal circulation.[68,69] It could be a strategic site to support newborn immune development, while bone marrow and the spleen progressively replace this function. Analysis of the splenic immune subsets in postnatal day 0 WT and *Pex2*$^{-/-}$ mice by flow cytometry analyses uncovered severe hematopoietic defects associated with *Pex2* deficiency. These defects were magnified among circulating populations. Although it was reported that few *Pex2*$^{-/-}$ mice could survive at least at postnatal day 10,[21] in our hands, the mice died at postnatal days 0–1. We speculate that the difference could be due to environmental differences caused by different animal houses.[70] In our study, we could differentiate *in vitro* cDCs or macrophages from bone marrow precursors of WT and *Pex2*$^{-/-}$ mice. However, the defects in the expression of MHC class II expression in BMDCs, which is a marker of differentiation, could not be rescued *in vitro*, suggesting that some differentiation processes are permanently affected and depend on peroxisome in a cell-autonomous way. Future studies to investigate the requirement for peroxisomes in hematopoiesis postbirth and at different hematopoietic sites should be conducted using conditional *Pex2* deletion models.

The identification of a requirement for peroxisome lipid metabolism in cDC expression of MHC class II has broad implications for host immunity. We demonstrated the impact of this defect, showing that antigen presentation activity by cDCs via MHC class II to CD4^{+} T cells is impaired.

Our findings shed light on the immune metabolic requirements of peroxisomes in immune cells. Our data also have an implication for a better understanding of DC development and function. Given the importance of DCs and their role in antigen presentation to T cells for vaccine efficacy, our study also enhances the importance of considering the peroxisome as a potential pharmacological target in future considerations for vaccine and adjuvant designs. Additionally, our data also contribute to the transcriptional signatures that identify neonatal hepatic immune cells and detail pathological features of PBD-ZSS that help better define this disease. These findings add to the growing list of peroxisome immunomodulatory functions and confirm the major role that peroxisomes play not only in innate immune cells but also in adaptive immunity, underlining the potential for using peroxisome function as markers or therapeutic targets in metabolic and immune disorders.

Limitations of the study

This study provides transcriptional signatures to identify the immune population at day 0 hepatic immune environment. A limitation of this study is that we could not perform scRNA-seq experiments after day 0, and therefore we could not record how the cell-specific gene signatures change over time. Our study provides the analysis of hematopoiesis in a severe PBD-ZSS model. Our data strongly suggest that severe defects in peroxisome biogenesis affect developmental hematopoiesis. However, we

studied a severe PBD-ZSS murine model that is lethal at days 0–1 postbirth in our hands. This phenotype's high penetrance and expressivity have been an obstacle to probing the hepatic immune environment at a later age and verifying whether the immune cell development is ultimately affected or only delayed. We found that bone marrow-derived cells can differentiate *in vitro* into macrophages[12] and DCs. However, the bone marrow-derived cells still present the differentiation defects observed in hepatic DCs, suggesting that distinct differentiation defects are intrinsic and are not caused by environment or developmental delay. A previous study reported that ablation of peroxisome functions only in the hematopoietic stem cells led to developmental and functional defects in innate B cell and T cell clonal expansion[16] but did not detect defects in follicular B or T cells. This discrepancy with our data could be due to differences in the gene mutation or temporal and spatial activation of the mutation. Further studies in various inducible and less severe global PBD-ZSS mice are necessary to define the requirement of peroxisome in hematopoiesis.

STAR★METHODS

Detailed methods are provided in the online version of this paper and include the following:

- KEY RESOURCES TABLE
- RESOURCE AVAILABILITY
  - Lead contact
  - Materials availability
  - Data and code availability
- EXPERIMENTAL MODEL AND STUDY PARTICIPANT DETAILS
  - Mammalian cells
- METHOD DETAILS
  - Reagents
  - Treatment with phorbol 12-myristate 13-acetate, 1,2-dioctanoyl-*sn*-glycerol or IFNγ of DCs
  - Multi-spectral imaging flow cytometry (IFC)
  - Internalization assay
  - Sample preparation for single-cell sequencing
  - Flow cytometry
  - Antigen presentation assay
  - RNA extraction and quantitative real-time PCR
  - Isolation of cell membranes
  - Quantification of diacylglycerol
  - PKC kinase activity assay
  - Immunofluorescence microscopy
  - Preparation of protein extracts for SDS–PAGE
  - Western blotting
- QUANTIFICATION AND STATISTICAL ANALYSIS
  - Statistical analysis
  - Quantification of immune fluorescence signals
  - Quantification of western blots signals

SUPPLEMENTAL INFORMATION

Supplemental information can be found online at https://doi.org/10.1016/j.celrep.2024.113744.

ACKNOWLEDGMENTS

Flow cytometry was performed at the Dalhousie University, Faculty of Medicine Flow Cytometry Core Facility. Microscopy was performed at the Dalhousie University, Faculty of Medicine Cellular and Molecular Digital Imaging. We thank Brianne Lindsay and Gerard Gaspard for their help with microscopy and Derek Rowter for training and technical assistance in flow cytometry. scRNA libraries were prepared at Princess Margaret Genomics Center for generation of 10× Genomics barcoded libraries and sequencing. This work was funded by a Project Grant from the Canadian Institutes of Health Research to F.D., a Discovery Grant from the Natural Sciences and Engineering Research Council of Canada to F.D., a Canada Foundation for Innovation JELF equipment grant to F.D., and the Dalhousie Medical Research Foundation start-up fund to F.D.

AUTHOR CONTRIBUTIONS

F.D., D.M.-L., and B.D.P. performed experiments using BMDCs and liver-derived immune cell extraction. R.A.C., G.S.G., and M.P. isolated CD45$^+$ cells for scRNA-seq. M.S. performed some of the flow cytometry analysis together with D.M.-L.; and B.D.P., A.P.M., S.S., and Y.H. advised on experiments using mice. Y.H. performed the antigen presentation assays. N.E.B. supplied cells from patients with PBDs. M.P. and R.A.C. established the *Pex2* mutant mouse colony and extracted immune cells from livers, spleens, peripheral blood, and bone marrow. J.F.R.-A. designed the RT-qPCR assays to detect MHC class II expression and, with E.L., advised on experiments to study antigen presentation. T.K.K. and I.H.I.A. assisted B.D.P. with the analyses. F.D. conceived the project, performed experiments and analyses, and wrote the manuscript with B.D.P.

DECLARATION OF INTERESTS

The authors declare no competing interests.

Received: November 10, 2023
Revised: December 21, 2023
Accepted: January 18, 2024

REFERENCES

1. Wanders, R.J.A., and Waterham, H.R. (2006). Biochemistry of mammalian peroxisomes revisited. Annu. Rev. Biochem. *75*, 295–332. https://doi.org/10.1146/annurev.biochem.74.082803.133329.
2. Wanders, R.J.A., Baes, M., Ribeiro, D., Ferdinandusse, S., and Waterham, H.R. (2023). The physiological functions of human peroxisomes. Physiol. Rev. *103*, 957–1024. https://doi.org/10.1152/physrev.00051.2021.
3. Smith, J.J., and Aitchison, J.D. (2013). Peroxisomes take shape. Nat. Rev. Mol. Cell Biol. *14*, 803–817. https://doi.org/10.1038/nrm3700.
4. Braverman, N.E., D'Agostino, M.D., and Maclean, G.E. (2013). Peroxisome biogenesis disorders: Biological, clinical and pathophysiological perspectives. Dev. Disabil. Res. Rev. *17*, 187–196. https://doi.org/10.1002/ddrr.1113.
5. Gilkrist, K.W., Opitz, J.M., Gilbert, E.F., Tsang, W., and Miller, P. (1974). Letter: Immunodeficiency in the cerebro-hepato-renal syndrome of Zellweger. Lancet *1*, 164–165.
6. Lucaccioni, L., Righi, B., Cingolani, G.M., Lugli, L., Della Casa, E., Torcetta, F., Iughetti, L., and Berardi, A. (2020). Overwhelming sepsis in a neonate affected by Zellweger syndrome due to a compound heterozygosis in PEX 6 gene: a case report. BMC Med. Genet. *21*, 229. https://doi.org/10.1186/s12881-020-01175-y.
7. Fazi, C., Lodi, L., Magi, L., Canessa, C., Giovannini, M., Pelosi, C., Pochiero, F., Procopio, E., Donati, M.A., Azzari, C., and Ricci, S. (2022). Case Report: Zellweger Syndrome and Humoral Immunodeficiency: The

Relevance of Newborn Screening for Primary Immunodeficiency. Front. Pediatr. *10*, 852943. https://doi.org/10.3389/fped.2022.852943.

8. Di Cara, F., Savary, S., Kovacs, W.J., Kim, P., and Rachubinski, R.A. (2023). The peroxisome: an up-and-coming organelle in immunometabolism. Trends Cell Biol. *33*, 70–86. https://doi.org/10.1016/j.tcb.2022.06.001.

9. Lodhi, I.J., Wei, X., Yin, L., Feng, C., Adak, S., Abou-Ezzi, G., Hsu, F.F., Link, D.C., and Semenkovich, C.F. (2015). Peroxisomal lipid synthesis regulates inflammation by sustaining neutrophil membrane phospholipid composition and viability. Cell Metabol. *21*, 51–64. https://doi.org/10.1016/j.cmet.2014.12.002.

10. Fletcher, J.M., Jordan, M.A., Snelgrove, S.L., Slattery, R.M., Dufour, F.D., Kyparissoudis, K., Besra, G.S., Godfrey, D.I., and Baxter, A.G. (2008). Congenic analysis of the NKT cell control gene Nkt2 implicates the peroxisomal protein Pxmp4. J. Immunol. *181*, 3400–3412. https://doi.org/10.4049/jimmunol.181.5.3400.

11. Di Cara, F., Sheshachalam, A., Braverman, N.E., Rachubinski, R.A., and Simmonds, A.J. (2017). Peroxisome-Mediated Metabolism Is Required for Immune Response to Microbial Infection. Immunity *47*, 93–106.e7. https://doi.org/10.1016/j.immuni.2017.06.016.

12. Nath, A.S., Parsons, B.D., Makdissi, S., Chilvers, R.L., Mu, Y., Weaver, C.M., Euodia, I., Fitze, K.A., Long, J., Scur, M., et al. (2022). Modulation of the cell membrane lipid milieu by peroxisomal beta-oxidation induces Rho1 signaling to trigger inflammatory responses. Cell Rep. *38*, 110433. https://doi.org/10.1016/j.celrep.2022.110433.

13. Dixit, E., Boulant, S., Zhang, Y., Lee, A.S.Y., Odendall, C., Shum, B., Hacohen, N., Chen, Z.J., Whelan, S.P., Fransen, M., et al. (2010). Peroxisomes are signaling platforms for antiviral innate immunity. Cell *141*, 668–681. https://doi.org/10.1016/j.cell.2010.04.018.

14. Vijayan, V., Srinu, T., Karnati, S., Garikapati, V., Linke, M., Kamalyan, L., Mali, S.R., Sudan, K., Kollas, A., Schmid, T., et al. (2017). A New Immunomodulatory Role for Peroxisomes in Macrophages Activated by the TLR4 Ligand Lipopolysaccharide. J. Immunol. *198*, 2414–2425. https://doi.org/10.4049/jimmunol.1601596.

15. Meghnem, D., Leong, E., Pinelli, M., Marshall, J.S., and Di Cara, F. (2022). Peroxisomes Regulate Cellular Free Fatty Acids to Modulate Mast Cell TLR2, TLR4, and IgE-Mediated Activation. Front. Cell Dev. Biol. *10*, 856243. https://doi.org/10.3389/fcell.2022.856243.

16. Muri, J., Corak, B., Matsushita, M., Baes, M., and Kopf, M. (2022). Peroxisomes Are Critical for the Development and Maintenance of B1 and Marginal Zone B Cells but Dispensable for Follicular B Cells and T Cells. J. Immunol. *208*, 839–850. https://doi.org/10.4049/jimmunol.2100518.

17. Biermanns, M., von Laar, J., Brosius, U., and Gärtner, J. (2003). The peroxisomal membrane targeting elements of human peroxin 2 (PEX2). Eur. J. Cell Biol. *82*, 155–162. https://doi.org/10.1078/0171-9335-00310.

18. Faust, P.L., and Hatten, M.E. (1997). Targeted deletion of the PEX2 peroxisome assembly gene in mice provides a model for Zellweger syndrome, a human neuronal migration disorder. J. Cell Biol. *139*, 1293–1305. https://doi.org/10.1083/jcb.139.5.1293.

19. Nakagaki, B.N., Mafra, K., de Carvalho, É., Lopes, M.E., Carvalho-Gontijo, R., de Castro-Oliveira, H.M., Campolina-Silva, G.H., de Miranda, C.D.M., Antunes, M.M., Silva, A.C.C., et al. (2018). Immune and metabolic shifts during neonatal development reprogram liver identity and function. J. Hepatol. *69*, 1294–1307. https://doi.org/10.1016/j.jhep.2018.08.018.

20. Liang, Y., Kaneko, K., Xin, B., Lee, J., Sun, X., Zhang, K., and Feng, G.S. (2022). Temporal analyses of postnatal liver development and maturation by single-cell transcriptomics. Dev. Cell *57*, 398–414.e5. https://doi.org/10.1016/j.devcel.2022.01.004.

21. Faust, P.L., Su, H.M., Moser, A., and Moser, H.W. (2001). The peroxisome deficient PEX2 Zellweger mouse: pathologic and biochemical correlates of lipid dysfunction. J. Mol. Neurosci. *16*, 289–321. https://doi.org/10.1385/JMN:16:2-3:289.

22. MacParland, S.A., Liu, J.C., Ma, X.Z., Innes, B.T., Bartczak, A.M., Gage, B.K., Manuel, J., Khuu, N., Echeverri, J., Linares, I., et al. (2018). Single cell RNA sequencing of human liver reveals distinct intrahepatic macrophage populations. Nat. Commun. *9*, 4383. https://doi.org/10.1038/s41467-018-06318-7.

23. Remmerie, A., Martens, L., Thoné, T., Castoldi, A., Seurinck, R., Pavie, B., Roels, J., Vanneste, B., De Prijck, S., Vanhockerhout, M., et al. (2020). Osteopontin Expression Identifies a Subset of Recruited Macrophages Distinct from Kupffer Cells in the Fatty Liver. Immunity *53*, 641–657.e14. https://doi.org/10.1016/j.immuni.2020.08.004.

24. Su, Q., Kim, S.Y., Adewale, F., Zhou, Y., Aldler, C., Ni, M., Wei, Y., Burczynski, M.E., Atwal, G.S., Sleeman, M.W., et al. (2021). Single-cell RNA transcriptome landscape of hepatocytes and non-parenchymal cells in healthy and NAFLD mouse liver. iScience *24*, 103233. https://doi.org/10.1016/j.isci.2021.103233.

25. Xiong, X., Kuang, H., Liu, T., and Lin, J.D. (2020). A Single-Cell Perspective of the Mammalian Liver in Health and Disease. Hepatology *71*, 1467–1473. https://doi.org/10.1002/hep.31149.

26. Wang, J., Hu, W., Shen, Z., Liu, T., Dai, W., Shen, B., Li, X., Wu, J., Lu, L., Li, S., and Cai, X. (2021). Dissecting the single-cell transcriptomeunderlying chronic liver injury. Mol. Ther. Nucleic Acids *26*, 1364–1373. https://doi.org/10.1016/j.omtn.2021.11.008.

27. Bjerregaard, M.D., Jurlander, J., Klausen, P., Borregaard, N., and Cowland, J.B. (2003). The in vivo profile of transcription factors during neutrophil differentiation in human bone marrow. Blood *101*, 4322–4332. https://doi.org/10.1182/blood-2002-03-0835.

28. Borregaard, N., and Cowland, J.B. (1997). Granules of the human neutrophilic polymorphonuclear leukocyte. Blood *89*, 3503–3521.

29. Alkhani, A., Korsholm, C., Levy, C.S., Mohamedaly, S., Duwaerts, C.C., Pietras, E.M., and Nijagal, A. (2023). Neonatal Hepatic Myeloid Progenitors Expand and Propagate Liver Injury in Mice. J. Clin. Med. *12*, 337. https://doi.org/10.3390/jcm12010337.

30. Yáñez, A., Coetzee, S.G., Olsson, A., Muench, D.E., Berman, B.P., Hazelett, D.J., Salomonis, N., Grimes, H.L., and Goodridge, H.S. (2017). Granulocyte-Monocyte Progenitors and Monocyte-Dendritic Cell Progenitors Independently Produce Functionally Distinct Monocytes. Immunity *47*, 890–902.e4. https://doi.org/10.1016/j.immuni.2017.10.021.

31. Villani, A.C., Satija, R., Reynolds, G., Sarkizova, S., Shekhar, K., Fletcher, J., Griesbeck, M., Butler, A., Zheng, S., Lazo, S., et al. (2017). Single-cell RNA-seq reveals new types of human blood dendritic cells, monocytes, and progenitors. Science *356*, eaah4573. https://doi.org/10.1126/science.aah4573.

32. Sprenkeler, E.G.G., Zandstra, J., van Kleef, N.D., Goetschalckx, I., Verstegen, B., Aarts, C.E.M., Janssen, H., Tool, A.T.J., van Mierlo, G., van Bruggen, R., et al. (2022). S100A8/A9 Is a Marker for the Release of Neutrophil Extracellular Traps and Induces Neutrophil Activation. Cells *11*. https://doi.org/10.3390/cells11020236.

33. Haage, V., Semtner, M., Vidal, R.O., Hernandez, D.P., Pong, W.W., Chen, Z., Hambardzumyan, D., Magrini, V., Ly, A., Walker, J., et al. (2019). Comprehensive gene expression meta-analysis identifies signature genes that distinguish microglia from peripheral monocytes/macrophages in health and glioma. Acta Neuropathol. Commun. *7*, 20. https://doi.org/10.1186/s40478-019-0665-y.

34. Hamey, F.K., Lau, W.W.Y., Kucinski, I., Wang, X., Diamanti, E., Wilson, N.K., Göttgens, B., and Dahlin, J.S. (2021). Single-cell molecular profiling provides a high-resolution map of basophil and mast cell development. Allergy *76*, 1731–1742. https://doi.org/10.1111/all.14633.

35. Choi, S.C., Wang, H., Tian, L., Murakami, Y., Shin, D.M., Borrego, F., Morse, H.C., 3rd, and Coligan, J.E. (2013). Mouse IgM Fc receptor, FCMR, promotes B cell development and modulates antigen-driven immune responses. J. Immunol. *190*, 987–996. https://doi.org/10.4049/jimmunol.1202227.

36. Muto, A., Ochiai, K., Kimura, Y., Itoh-Nakadai, A., Calame, K.L., Ikebe, D., Tashiro, S., and Igarashi, K. (2010). Bach2 represses plasma cell gene

regulatory network in B cells to promote antibody class switch. EMBO J. *29*, 4048–4061. https://doi.org/10.1038/emboj.2010.257.

37. Rugh, R. (1990). The Mouse: Its Reproduction and Development (Oxford University Press).
38. Abbas, A., Vu Manh, T.P., Valente, M., Collinet, N., Attaf, N., Dong, C., Naciri, K., Chelbi, R., Brelurut, G., Cervera-Marzal, I., et al. (2020). The activation trajectory of plasmacytoid dendritic cells in vivo during a viral infection. Nat. Immunol. *21*, 983–997. https://doi.org/10.1038/s41590-020-0731-4.
39. Zhang, J., Raper, A., Sugita, N., Hingorani, R., Salio, M., Palmowski, M.J., Cerundolo, V., and Crocker, P.R. (2006). Characterization of Siglec-H as a novel endocytic receptor expressed on murine plasmacytoid dendritic cell precursors. Blood *107*, 3600–3608. https://doi.org/10.1182/blood-2005-09-3842.
40. Valente, M., Collinet, N., Vu Manh, T.P., Popoff, D., Rahmani, K., Naciri, K., Bessou, G., Rua, R., Gil, L., Mionnet, C., et al. (2023). Novel mouse models based on intersectional genetics to identify and characterize plasmacytoid dendritic cells. Nat. Immunol. *24*, 714–728. https://doi.org/10.1038/s41590-023-01454-9.
41. Jiang, Y., Tang, Y., Hoover, C., Kondo, Y., Huang, D., Restagno, D., Shao, B., Gao, L., Michael McDaniel, J., Zhou, M., et al. (2021). Kupffer cell receptor CLEC4F is important for the destruction of desialylated platelets in mice. Cell Death Differ. *28*, 3009–3021. https://doi.org/10.1038/s41418-021-00797-w.
42. Wangler, M.F., Chao, Y.H., Bayat, V., Giagtzoglou, N., Shinde, A.B., Putluri, N., Coarfa, C., Donti, T., Graham, B.H., Faust, J.E., et al. (2017). Peroxisomal biogenesis is genetically and biochemically linked to carbohydrate metabolism in Drosophila and mouse. PLoS Genet. *13*, e1006825. https://doi.org/10.1371/journal.pgen.1006825.
43. Chang, C.H., Guerder, S., Hong, S.C., van Ewijk, W., and Flavell, R.A. (1996). Mice lacking the MHC class II transactivator (CIITA) show tissue-specific impairment of MHC class II expression. Immunity *4*, 167–178. https://doi.org/10.1016/s1074-7613(00)80681-0.
44. Facciotti, F., Ramanjaneyulu, G.S., Lepore, M., Sansano, S., Cavallari, M., Kistowska, M., Forss-Petter, S., Ni, G., Colone, A., Singhal, A., et al. (2012). Peroxisome-derived lipids are self antigens that stimulate invariant natural killer T cells in the thymus. Nat. Immunol. *13*, 474–480. https://doi.org/10.1038/ni.2245.
45. Kwon, M.J., Yao, Y., Walter, M.J., Holtzman, M.J., and Chang, C.H. (2007). Role of PKCdelta in IFN-gamma-inducible CIITA gene expression. Mol. Immunol. *44*, 2841–2849. https://doi.org/10.1016/j.molimm.2007.01.035.
46. Wu, X., Kong, X., Luchsinger, L., Smith, B.D., and Xu, Y. (2009). Regulating the activity of class II transactivator by posttranslational modifications: exploring the possibilities. Mol. Cell Biol. *29*, 5639–5644. https://doi.org/10.1128/MCB.00661-09.
47. Majewski, M., Bose, T.O., Sillé, F.C.M., Pollington, A.M., Fiebiger, E., and Boes, M. (2007). Protein kinase C delta stimulates antigen presentation by Class II MHC in murine dendritic cells. Int. Immunol. *19*, 719–732. https://doi.org/10.1093/intimm/dxm034.
48. Steinberg, S.F. (2008). Structural basis of protein kinase C isoform function. Physiol. Rev. *88*, 1341–1378. https://doi.org/10.1152/physrev.00034.2007.
49. Eichmann, T.O., and Lass, A. (2015). DAG tales: the multiple faces of diacylglycerol–stereochemistry, metabolism, and signaling. Cell. Mol. Life Sci. *72*, 3931–3952. https://doi.org/10.1007/s00018-015-1982-3.
50. Li, W., Zhang, J., Bottaro, D.P., and Pierce, J.H. (1997). Identification of serine 643 of protein kinase C-delta as an important autophosphorylation site for its enzymatic activity. J. Biol. Chem. *272*, 24550–24555. https://doi.org/10.1074/jbc.272.39.24550.
51. Demarquoy, J., and Le Borgne, F. (2015). Crosstalk between mitochondria and peroxisomes. World J. Biol. Chem. *6*, 301–309. https://doi.org/10.4331/wjbc.v6.i4.301.
52. Ganong, B.R., Loomis, C.R., Hannun, Y.A., and Bell, R.M. (1986). Specificity and mechanism of protein kinase C activation by sn-1,2-diacylglycerols. Proc. Natl. Acad. Sci. USA *83*, 1184–1188. https://doi.org/10.1073/pnas.83.5.1184.
53. Ebeling, J.G., Vandenbark, G.R., Kuhn, L.J., Ganong, B.R., Bell, R.M., and Niedel, J.E. (1985). Diacylglycerols mimic phorbol diester induction of leukemic cell differentiation. Proc. Natl. Acad. Sci. USA *82*, 815–819. https://doi.org/10.1073/pnas.82.3.815.
54. Steimle, V., Siegrist, C.A., Mottet, A., Lisowska-Grospierre, B., and Mach, B. (1994). Regulation of MHC class II expression by interferon-gamma mediated by the transactivator gene CIITA. Science *265*, 106–109. https://doi.org/10.1126/science.8016643.
55. Muhlethaler-Mottet, A., Di Berardino, W., Otten, L.A., and Mach, B. (1998). Activation of the MHC class II transactivator CIITA by interferon-gamma requires cooperative interaction between Stat1 and USF-1. Immunity *8*, 157–166. https://doi.org/10.1016/s1074-7613(00)80468-9.
56. Muhlethaler-Mottet, A., Otten, L.A., Steimle, V., and Mach, B. (1997). Expression of MHC class II molecules in different cellular and functional compartments is controlled by differential usage of multiple promoters of the transactivator CIITA. EMBO J. *16*, 2851–2860. https://doi.org/10.1093/emboj/16.10.2851.
57. Salles, A., Billaudeau, C., Sergé, A., Bernard, A.M., Phélipot, M.C., Bertaux, N., Fallet, M., Grenot, P., Marguet, D., He, H.T., and Hamon, Y. (2013). Barcoding T cell calcium response diversity with methods for automated and accurate analysis of cell signals (MAAACS). PLoS Comput. Biol. *9*, e1003245. https://doi.org/10.1371/journal.pcbi.1003245.
58. Rosewich, H., Ohlenbusch, A., and Gärtner, J. (2005). Genetic and clinical aspects of Zellweger spectrum patients with PEX1 mutations. J. Med. Genet. *42*, e58. https://doi.org/10.1136/jmg.2005.033324.
59. Cardoso, P., Amaral, M.E., Lemos, S., and Garcia, P. (2016). Zellweger syndrome with severe malnutrition, immunocompromised state and opportunistic infections. BMJ Case Rep. *2016*, bcr2015214283. https://doi.org/10.1136/bcr-2015-214283.
60. Magnuson, N.S., and Perryman, L.E. (1986). Metabolic defects in severe combined immunodeficiency in man and animals. Comp. Biochem. Physiol. B *83*, 701–710. https://doi.org/10.1016/0305-0491(86)90134-3.
61. Althonaian, N., Alsultan, A., Morava, E., and Alfadhel, M. (2018). Secondary Hemophagocytic Syndrome Associated with COG6 Gene Defect: Report and Review. JIMD Rep. *42*, 105–111. https://doi.org/10.1007/8904_2018_88.
62. Barnabei, L., Laplantine, E., Mbongo, W., Rieux-Laucat, F., and Weil, R. (2021). NF-kappaB: At the Borders of Autoimmunity and Inflammation. Front. Immunol. *12*, 716469. https://doi.org/10.3389/fimmu.2021.716469.
63. Bros, M., Haas, K., Moll, L., and Grabbe, S. (2019). RhoA as a Key Regulator of Innate and Adaptive Immunity. Cells *8*. https://doi.org/10.3390/cells8070733.
64. Biro, M., Munoz, M.A., and Weninger, W. (2014). Targeting Rho-GTPases in immune cell migration and inflammation. Br. J. Pharmacol. *171*, 5491–5506. https://doi.org/10.1111/bph.12658.
65. Lekstrom-Himes, J.A., and Gallin, J.I. (2000). Immunodeficiency diseases caused by defects in phagocytes. N. Engl. J. Med. *343*, 1703–1714. https://doi.org/10.1056/NEJM200012073432307.
66. Chen, K., Zhang, N., Shao, J.B., Li, H., Li, J., Xi, J.M., Xu, W.H., and Jiang, H. (2021). Allogeneic Hematopoietic Stem Cell Transplantation for PEX1-Related Zellweger Spectrum Disorder: A Case Report and Literature Review. Front. Pediatr. *9*, 672187. https://doi.org/10.3389/fped.2021.672187.
67. Shapiro, E., Krivit, W., Lockman, L., Jambaqué, I., Peters, C., Cowan, M., Harris, R., Blanche, S., Bordigoni, P., Loes, D., et al. (2000). Long-term effect of bone-marrow transplantation for childhood-onset cerebral X-linked adrenoleukodystrophy. Lancet *356*, 713–718. https://doi.org/10.1016/S0140-6736(00)02629-5.

68. Tripathi, A., Debelius, J., Brenner, D.A., Karin, M., Loomba, R., Schnabl, B., and Knight, R. (2018). The gut-liver axis and the intersection with the microbiome. Nat. Rev. Gastroenterol. Hepatol. *15*, 397–411. https://doi.org/10.1038/s41575-018-0011-z.

69. Gola, A., Dorrington, M.G., Speranza, E., Sala, C., Shih, R.M., Radtke, A.J., Wong, H.S., Baptista, A.P., Hernandez, J.M., Castellani, G., et al. (2021). Commensal-driven immune zonation of the liver promotes host defence. Nature *589*, 131–136. https://doi.org/10.1038/s41586-020-2977-2.

70. Kawakami, K., Matsuo, H., Kajitani, N., Yamada, T., and Matsumoto, K.I. (2022). Comparison of survival rates in four inbred mouse strains under different housing conditions: effects of environmental enrichment. Exp. Anim. *71*, 150–160. https://doi.org/10.1538/expanim.21-0118.

71. McInnes, L., Healy, J., Saul, N., and Großberger, L. (2018). UMAP: Uniform Manifold Approximation and Projection. Journal of Open Source Software *5*, 861. https://doi.org/10.21105/joss.00861.

72. Schneider, C., Rasband, W., and Eliceiri, K. (2012). NIH Image to ImageJ: 25 years of image analysis. Nat. Methods *9*, 671–675. https://doi.org/10.1038/nmeth.2089.

73. Reimand, J., Isserlin, R., Voisin, V., Kucera, M., Tannus-Lopes, C., Rostamianfar, A., Wadi, L., Meyer, M., Wong, J., Xu, C., et al. (2019). Pathway enrichment analysis and visualization of omics data using g:Profiler, GSEA, Cytoscape and EnrichmentMap. Nat. Protoc. *14*, 482–517. https://doi.org/10.1038/s41596-018-0103-9.

STAR★METHODS

KEY RESOURCES TABLE

REAGENT or RESOURCE	SOURCE	IDENTIFIER
Antibodies		
CD45	Biolegend	103136
CD11b	Biolegend	101216
Ly6C	Biolegend	128033
Ly6G	Biolegend	127627
MHC-II (I-A/I-E)	ThermoFischer	17-5321-81
CD103	ThermoFischer	12-1031-82
CD103	Biolegend	121419
Ftl3 (CD135)	Biolegend	135306
F4/80	Biolegend	157305
CD11c	Biolegend	117305
CD19	Biolegend	152407
CD3e	Biolegend	100327
NK1.1	Biolegend	156514
IgM	ThermoFischer	48-5890-82
MHC-II (I-A/I-E)	Biolegend	107631
CD8a AF 647	Ebioscience	Clone 53–6.7
H2Kb AF 647	Biolegend	Clone AF6-88.5
I-A/I-E AF 647	Becton Dickinson	Clone M5/114.15.2
CD54 (ICAM1) APC	Biolegend	Clone YN1/1.7.4
CD80 (B7-1) PE	Becton Dickinson	Clone 16-10A1
CD11c PE-Cy7	Biolegend	Clone N418
PKC-d	CellSignaling	D10E2
P-PKC-d	CellSignaling	Ser643/676
α-tubulin	Sigma-Aldrich	T5168
Ciita	Thermo Fisher Scientific	PA5-101105
Chemicals, peptides, and recombinant proteins		
BD PBX	Becton Dickinson	640175
OVA (257–264)	Eurogentec (Anaspec)	AS-60193-5
OVA (323–339)	Invivogen	Vac-isq
Lipopolysaccharides from Escherichia coli O55:B5	Sigma	L2880-25MG
PBS 10 X	thermofisher	70011044
Recombinant Murine GM-CSF 20μg	PeproTech	315–03
Recombinant Murine IL-4 20μg	PeproTech	214–14
Critical commercial assays		
MiniMACS™ Separator and Starting Kit	Miltenyi Biotec. Inc	NA
NexteraXT tagmentation kit	Illumina Inc	FC-131-1024
surface-bound Alexa Fluor488-labelled OVA	Invitrogen	11539176
Phorbol 12-myristate 13-acetate	Sigma–Aldrich	524400
1,2-dioctanoyl-*sn*-glycerol	Sigma–Aldrich	317505
RPMI, glutamax 1%	Cytiva	SH300096.01
IFNγ	eBioscience	575308
Trizol	Thermo Fisher Scientific	15596018

(*Continued on next page*)

Continued

REAGENT or RESOURCE	SOURCE	IDENTIFIER
Direct-zol™ RNA MicroPrep (200 Preps) w/Zymo-Spin™ IC Columns	Cedarlane	R2062
PKC Kinase Activity Assay Kit	Abcam	AB139437
Diacylglycerol Assay Kit	Abcam	AB242293-1001
1 x Complete Protease Inhibitor	Roche	11697498001
PhoStop	Roche	4906837001
PowerTrack SYBR Green Master Mix	Applied Biosystems	A46109
High-Capacity cDNA Reverse Transcription Kit with RNase Inhibitor	Applied Biosystems	4374966
Pierce™ 16% Formaldehyde (w/v), Methanol-free	Thermo Fisher Scientific	28906
Fetal bovine serum	Thermo Fisher Scientific	10270106
Penicillin-Streptomycin	Thermo Fisher Scientific	15140122
Deposited data		
scRNA sequencing data	This study	GSE248598
Experimental models: Cell lines		
Mouse: Bone marrow derived macrophages from Sw129-Pxmp3^{tm1Plf}−/−Mutant Mouse Resource and MMRRC	Research Center (MMRRC) supported by the NIH	Faust and Hatten, 1997[18]
Mouse: Bone marrow derived dendritic cells from Sw129-Pxmp3^{tm1Plf}−/+	Research Center (MMRRC) supported by the NIH	Faust and Hatten, 1997[18]
MutuDC1	Gift from Yannick Hamon, CENTER D'IMMUNOLOGIE MARSEILLE	NA
Experimental models: Organisms/strains		
129S6.129-Pex2^{tm1Plf}/Mmmh	Mutant Mouse Resource and Research Center	Faust and Hatten, 1997[18]
Swiss Webster	Charles River	024
OT-II mouse	JAX	003831
Oligonucleotides		
Hprt, forward 5′-TGAAGTACTCATTATA GTCAAGGGCA-3′	Di Cara Dalhousie University (This paper)	NA
Hprt, reverse 5′-CTGGTGAAAAGGACC TCTCG-3′;	Di Cara Dalhousie University (This paper)	NA
Ciita forward 5′-CCCTGCGTGTGATGG ATGTC-3′	Di Cara Dalhousie University (This paper)	NA
Ciita reverse 5′-ATCTCAGACTGATCC TGGCAT-3′	Di Cara Dalhousie University (This paper)	NA
H2-Aa forward 5′-CAACCGTGACTATT CCTTCC-3′	Di Cara Dalhousie University (This paper)	NA
H2-Aa reverse 5′-CCACAGTCTCTGTC AGCTC-3′	Di Cara Dalhousie University (This paper)	NA
H2-Ab1 forward 5′-GTGTGCAGACACA ACTACGAGG-3′	Di Cara Dalhousie University (This paper)	NA
H2-Ab1 reverse 5′-CTGTCACTGAGCA GACCAGAGT-3′	Di Cara Dalhousie University (This paper)	NA
H2-DMb1 forward 5′-AGCCTTCTCCA GCGTTTGC-3′	Di Cara Dalhousie University (This paper)	NA
H2-DMb1 reverse 5′-TTTGGGCTACTC GGACAGATG-3′	Di Cara Dalhousie University (This paper)	NA

(*Continued on next page*)

Continued

REAGENT or RESOURCE	SOURCE	IDENTIFIER
Software and algorithms		
R version 4.0.4	https://www.r-project.org	NA
Python 3.7	https://www.python.org	McInnes et al., 2020[71]
FIJI/ImageJ software	https://imagej.nih.gov/ij/	Schneider et al., 2012[72]
GraphPad 6	Prism	NA
Cytoscape	NA	Reimand et al., 2019[73]
Zeiss Zen lite Black & lite Blue	Zeiss	https://www.zeiss.com/microscopy/int/products/microscope-software/zen-lite.
FloJo	BD	NA
IDEAS software	Millipore	https://www.emdmillipore.com/CA/en/20150212_144049
Others		
observation chamber	Labtek	NA

RESOURCE AVAILABILITY

Lead contact

Further information and requests for resources and reagents should be directed to and will be fulfilled by the lead contact, Francesca Di Cara (dicara@dal.ca).

Materials availability

No new reagent or animal model was generated in this study.

Data and code availability

- All sequencing data have been uploaded to the NCBI GEO database and can be accessed via the project accession number GSE248598.
- This paper does not report original code
- Any additional information required to reanalyze the data reported in this paper is available from the lead contact upon request.

EXPERIMENTAL MODEL AND STUDY PARTICIPANT DETAILS

Mammalian cells

Murine bone marrow-derived macrophages

Murine bone marrow-derived monocytes were extracted from male and female 1-day-old pups, differentiated into macrophages (BMDMs), and treated as previously described (Geng et al., 2015).

Murine bone marrow-derived dendritic cells

Bone marrow hematopoietic cell progenitors were differentiated into dendritic cells in RPMI, glutamax 1%, 10% Fetal calf serum, penicillin/streptomycin (1%) supplemented with GM-CSF (# 315-03 PeproTech, 20 μg/ml) for three days following recovery at 37°C, 5% CO_2. The culture medium was changed every two days. Cells were split before they reached 80% confluency at each passage. Cells were harvested using gentle non-enzymatic cell dissociation reagent (PBS 1X, EDTA 0.5mM) and pulled together with cells in suspension. All cells were spun down and resuspended in a complete medium supplemented with 10 μg/ml GM-CSF for five days, followed by a two days period where IL-4 (10μg/ml214-14 PreproTech) was added in addition to GM-CSF. Before flow cytometry, bone marrow-derived dendritic cells (BMDC) were splatted and divided into two plates. Cells in one dish were treated with the required stimuli.

Human peripheral blood mononuclear cells

Peripheral blood mononuclear cells (PBMCs) from 0 to 6-month-old healthy males or female patients affected by PBD-ZSS were provided by Dr. Nancy Braverman, McGill University (REB#). Frozen cell stocks were thawed and grown in RPMI medium (Gibco) supplemented with 10% heat-inactivated fetal bovine serum (HI FBS) (Hyclone, Thermo Scientific), 2 mM *L*-glutamine (Gibco), 50 mM 2-mercaptoethanol, 50 U penicillin/mL, 50 μg streptomycin sulfate/mL.

Pex2 mutant mice

The *Pex2* mutant mouse strain used was 129S6.129-*Pex2*^{tm1Plf}/Mmmh (null allele).

Faust and Hatten, 1997) were obtained from the Mutant Mouse Resource & Research Centers (MMRRC) supported by the National Institutes of Health. The mice used for the experiments reported herein were *Pex2*$^{+/+}$, *Pex2*$^{-/-}$, and *Pex2*$^{+/-}$. Homozygous null mutants showed no Pex2 transcript and no Pex2 protein. Homozygous null mutants in the congenic strain 129S6.129-*Pex2*$^{tm1Plf\ +/-}$ showed variable embryonic lethality, starting at ~E11. Approximately 20% of homozygous null mutants survived to birth but were hypotonic, did not feed, and died on the day of birth. Homozygous null mutant mice that survived into the postnatal period were obtained by mating congenic 129S6.129-*Pex2*$^{tm1Plf\ +/-}$ mice with wild-type Swiss Webster strain mice. F1-*Pxmp3*$^{tm1Plf\ +/-}$ hybrids (designated Sw129) were then intercrossed to obtain Sw129-*Pxmp3*$^{tm1Plf\ -/-}$ (indicated in the text as *Pex2*$^{-/-}$) mice. Colonies were maintained as stable inbred lines in the Swiss Webster and 129SVEV backgrounds under approved animal protocol #21–023, abiding by the Canadian Council on Animal Care standards. The absence of peroxisomal matrix import in the homozygous mutant of this mouse strain was previously confirmed by our group.[12]

Equal number of males and females mice were used in each experiment.

METHOD DETAILS

Reagents

Rabbit antibodies to PKC-δ (D10E2) and P-PKC-δ (Ser643/676) were from Cell Signaling.

The mouse antibody to α-tubulin (T5168) was from Sigma-Aldrich.

The mouse antibody to CIITA (PA5-101105) was from Thermo Fisher Scientific.

Alexa Fluor 488-conjugated, and Alexa Fluor 555-conjugated donkey anti-mouse or donkey anti-rabbit secondary antibodies were from Abcam.

Phorbol 12-myristate 13-acetate (PMA)(#524400) and 1,2-dioctanoyl-*sn*-glycerol (#317505) were from Sigma–Aldrich and IFNγ (#575308) was from eBioscience.

Lipopolysaccharides from Escherichia coli O55:B5 (#L2880-25MG) were from Sigma-Aldrich. RPMI 1640 media was from Cytiva (SH300096.01) and RPMI was supplemented with 1% GlutaMAX (Gibco; #35050061).

Treatment with phorbol 12-myristate 13-acetate, 1,2-dioctanoyl-*sn*-glycerol or IFNγ of DCs

Differentiated WT and Pex2$^{-/-}$ BMDCs were incubated for 1 h with 25 ng/mL phorbol 12-myristate 13-acetate (PMA) (Sigma–Aldrich #524400), 10 μM 1,2-dioctanoyl-*sn*-glycerol (Sigma–Aldrich #317505) or with 100 ng/mL IFNγ (eBioscience #575,308) for 24 h and stimulated with LPS 100 ng/mL in 3-h experiment at 37°C, BMDCs were harvested in Trizol for RNA extraction fixed in 4% formaldehyde for immunofluorescence experiments or collected in PBS 1X, EDTA 5mM non enzymatic treatment and further labeled for flow cytometry.

Multi-spectral imaging flow cytometry (IFC)

To perform IFC, 10^{10} Alexa Fluor488-labelled -OVAII was added to 10^6 BMDCs and the combined cells were incubated for 15 min at 4°C to allow for Alexa Fluor488-labelled -OVA-cell contact and then incubated for 2 h at 37°C in Cell Culture Medium. DNA was detected by staining with Hoechst 33342. Data were acquired on an ImageStream Imaging Flow Cytometer (Amnis) (Rieger et al., 2010). Cells were analyzed *post hoc*.

Internalization assay

The number of Alexa Fluor488-labelled BMDCs cells was determined for each population by comparing the percentage of cells with internalized Alexa Fluor488-labelled OVA (Invitrogen #11539176) to the rate of cells with surface-bound Alexa Fluor488-labelled OVA. Using IDEAS software (Millipore), a mask was created to identify the eukaryotic cell membrane using the bright field signal for two sets of samples and cell tracker dye for two other groups of samples. This allowed differentiation between internalized (degree of internalization greater than 0) and bound (degree of internalization less than 0) Alexa Fluor 488 particles in the *x*-*y* axes and on the *z* axis.

Sample preparation for single-cell sequencing

Postnatal day-0 mice from three genotypes (*Pex2*$^{-/-}$, *Pex2*^{Het}, and WT) were euthanized by decapitation, their livers were excised and passed through a 70 μm cell strainer (Falcon Cat#352350) into 1x HBSS using a 1 mL syringe plunger. Liver cell suspensions were then centrifuged at 20 xg for 5 min to remove hepatocytes. The supernatant was isolated and ACK lysis was performed to lyse red blood cells. The final cell suspension was resuspended in 1x PBS 0.5% BSA, cell counts were determined and cells surface-stained for flow cytometry using a 1:50 dilution of FITC- and ef450-conjugated anti-CD45 antibodies and staining with a fixable viability dye (ThermoFisher eBioscience Cat#65–0865). Viable CD45$^+$ cells were sorted on a BD FACs ARIA II cell sorter. Sorted CD45$^+$ cells were then processed and fixed according to the 10X Genomics Flex Assay protocol. Fixed cells were counted and stored at −80°C and shipped on dry ice to the Princess Margaret Genomics Center for generation of 10X Genomics barcoded libraries and sequencing. Cell count determined for each genotype prior to sequencing were: 1.46x10^6 cells from WT, 1.45 and 3.06x10^5 from *Pex2*$^{-/-}$ mice, and 1.3 and 3.93 x10^5 from *Pex2*^{Het} mice. Samples were sequenced on an NovaSeq X Plus at a median sequencing depth of 50,000 reads per cell. Sequences were mapped to the mouse (mm10) genome using the cell ranger multi pipeline in Cell Ranger v.7.0.0.

Single-cell RNA sequencing analysis

Analysis of single-cell transcriptome gene expression was performed using 10x Genomics Loupe Browser v7.0. Low-quality cells and genes were filtered for downstream analysis. Analysis of single-cell transcriptome gene expression was performed using 10x Genomics Loupe Browser v7.0. Low-quality cells and genes were filtered for downstream analysis. We performed stringent filtering to ensure only high-quality data were retained for downstream analysis. We excluded cells expressing less than 700 genes across all conditions as well as those with high mitochondrial count (cutoff off 10%). Duplicate cells were also eliminated by maintaining an upper gene count cut off of (8000 counts). Consequently, a total of 34,895 cells passed this filtering criterion equating 95.3% rate or retention. We then performed dimensionality reduction and unsupervised clustering using UMAP. Cluster identification was guided using a K-Means of 10 clusters. Based on these clusters cell types were assigned manually following significant literature evaluation of cluster marker genes.[19,20] Subpopulations within each cell type (e.g., distinction of cDC1, cDC2, pDC, and MDP as subpopulations of DCs) were defined by first segregating each cell type cluster from the total cell population and then re-clustering to identify additional subclusters. Differential expression analysis was performed between assigned cell type clusters where a subset of 5–10 of the top differentially expressed genes (DEGs) and established cell type markers defined each cell type cluster. The log2 fold-change values of selected DEGs and cell assignments were hierarchically clustered and visualized by heatmap (Morpheus, https://software.broadinstitute.org/morpheus). To identify DEGs between WT, HET and KO samples, a pseudo-bulk differential expression analysis was performed using Loupe Browser 7.0.0. In brief, DEGs with >1.5 log-fold change between cell types of each genotype were assessed.

Single-cell enrichment pathway

Gene Set Enrichment Analysis (GSEA) was performed using GSEA v4.1.0 to identify biological processes, cellular components, and KEGG pathways significantly altered in the hepatic immune cells of *Pex2*$^{-/-}$ mice versus WT mice. The gene interaction network of GSEA results was generated and manually curated to remove redundant and uninformative nodes using Cytoscape v3.8.2.[73]

Flow cytometry

Postnatal day-0 mice were euthanized by decapitation, their livers were excised and passed through a 70 μm cell strainer (Falcon Cat#352350) into 1x HBSS using a 1 mL syringe plunger. Liver cell suspensions were then centrifuged at 20 xg for 5 min to remove hepatocytes. The supernatant was isolated and ACK lysis was performed to lyse red blood cells. The final cell suspension was resuspended in 1x PBS, cell counts were determined and then surface-stained for flow cytometry. Single-cell suspensions were stained with antibodies and stains listed. After gating out doublets CD45^{+} and fixable viability dye negative cells (ThermoFisher eBioscience Cat#65–0865) were gated by to their respective immune cell types as indicated. All samples were acquired on a BD-LSR Fortessa cytometer. For staining of bone marrow-derived cells for flow cytometry, cells were collected by 1x PBS, 5 mM EDTA nonenzymatic treatment. Cells were first surface stained for 45 min on ice with antibodies, washed twice in 1x PBS and further analyzed by flow cytometry on a FACSymphony cell analyzer (Becton Dickinson). Post-acquisition, after gating out doublets and cell debris, cells were reported in Figure S4.

Antigen presentation assay

OT-II CD4^{+} T cell cytosolic calcium fluxes were measured according to the ‘‘methods for automated and accurate analysis of cell signals’’ (MAAACS) developed by the co-author Dr. Hamon and extensively described in.[57] In brief, according to the manufacturer’s instructions, T cells were loaded with PBX calcium reporter (BD) diluted in 1X dye loading solution at 37°C for 1 h in the dark. Next, cells were washed twice by gentle centrifugation and resuspended in Hank’s balanced salt solution buffered with HEPES (1mM) (HBSS-H). They were then introduced in the desired observation chamber (Labtek) where BMDC or MutuDC1 were previously seeded 2 two days prior experiment and ON loaded with various OVA concentrations). Analysis was performed on a Zeiss LSM 780 confocal microscope equipped with a C-Apochromat 40X/1.2 water immersion objective and an argon laser with a 488 nm dichroic and a 505–530 nm band-pass filter. A temperature control system was used to ensure that 37°C was maintained during the entire acquisition. Time-lapse movies were typically made of 600 images taken every 7 s (with a pinhole set to 4 airy units), while cells were kept at 37°C using a hot plate.

RNA extraction and quantitative real-time PCR

Cells were rinsed twice with PBS, transferred to TRIzol reagent, and snap-frozen in liquid nitrogen. Total RNA was extracted using the Direct-Zol RNA micro prep (Cedarlane), according to the supplied protocol. RNA was reverse transcribed using 1) the High-capacity cDNA reverse transcription Kit (Applied Biosystems), and the synthesized cDNA was used for qPCR using the Power Track SYBR-Green PCR master mix (Applied Biosystems) and a QuantStudio 6 Flex Real-Time PCR system (Applied Biosystems). Samples were normalized to *Hprt* gene expression for mouse experiments using the relative quantification methods and primer efficiency. Primer sequences used in real-time qPCR are presented in the Key resources table.

Isolation of cell membranes

Cells were isolated in 0.25 M STKM buffer (0.25 M sucrose, 25 mM HEPES-KOH, pH 7.4, 25 mM KOAc, 5 mM $MgCl_2$, 0.1 mM EDTA, 1 x Complete Protease Inhibitor (Roche), 1 mM DTT) and sonicated in a sonicator bath to yield lysates. Lysates were centrifuged at 1,000 x *g* for 10 min at 4°C. The supernatant from this first spin was centrifuged at 10,000 x *g* for 20 min at 4°C. The supernatant from

this second spin containing fragmented membranes was centrifuged at 100,000 x *g* at 4°C for 1 h. The resultant pellets were resuspended in 0.25 M STKM and used for lipid assay.

Quantification of diacylglycerol

Diacylglycerol quantification was done using the Diacylglycerol Assay Kit (Abcam AB242293-1001) following the manufacturer's protocol.

Lipid amounts were normalized to cell number and protein amount.

PKC kinase activity assay

PKC kinase activity was measured using the PKC Kinase Activity Assay Kit (Abcam AB139437) following the manufacturer's protocol. Kinase activity was normalized to cell number and protein amount.

Immunofluorescence microscopy

Cells were fixed in 4% paraformaldehyde in PBS for 30 min, then incubated for 1 h at room temperature in 5% normal goat serum in 1x PBS and for 16 h at 4°C with primary antibody at a 1:100 dilution in 5% normal goat serum in 1x PBS. Appropriate Alexa Fluor secondary antibodies were then used at 1:1000 dilution in 5% normal goat serum, while Cy5 fluorescently labeled phalloidin was added to stain the cytoskeleton. After 4 washes in PBST (PBS +0.1% (v/v) Triton X-100), cells were mounted in DAPI Pro-Gold Antifade Reagent (Thermo Fisher) and imaged using a 63x oil immersion objective (NA = 1.4) using a Zeiss AxioObserver LSM 880 Airyscan, 63x 1.4 oil plan-Apochromat lens.

Preparation of protein extracts for SDS–PAGE

Cold lysis buffer (70 μL) (Ephrussi-Beadle Ringer's solution containing 10 mM EDTA, 10 mM dithiothreitol (DTT), and Roche complete protease and phosphatase inhibitors) was added to a pellet containing 200,000 DCs cells, which was then homogenized. Thirty microliters of hot (70°C) 3 × SDS–PAGE sample buffer containing 10 mM DTT was added to the homogenate, followed by boiling for 10 min. Particulate matter was pelleted by centrifugation at 16,000 × *g* for 1 min, and the supernatant was transferred to a fresh tube for analysis by SDS–PAGE.

Western blotting

Protein was resolved by 10% SDS–PAGE and transferred to nitrocellulose membranes. Membranes were blocked with 5% bovine serum albumin (BSA) or 5% nonfat dry milk for 1 h at room temperature, incubated for 16 h with primary antibody (1:1000 final dilution in TBST [150 mM NaCl, 20 mM Tris-HCl, pH 7.5, 0.05% Tween 20]) and washed three times for 5 min each with TBST. The washed membranes were incubated with an appropriate secondary antibody for 1 h at room temperature. Membranes were then washed three times for 5 min each with TBS containing 0.2% Triton X-100, and immunocomplexes were detected by enhanced chemiluminescence (ECL; Bio-Rad) using an appropriate horseradish peroxidase–linked secondary antibody (Amersham Biosciences) and developed using a.

ChemiDoc Imaging System (Bio-Rad).

QUANTIFICATION AND STATISTICAL ANALYSIS

Statistical analysis

Prism was used to generate graphs and quantify p values using statistical methods as indicated in the respective figure legends. Tests, numbers of experiments, error bars, and meaning of p values are shown in each figure legend.

Quantification of immune fluorescence signals

To determine the intensity of the defined protein within the cell.

(1) Open the ImageJ software.
(2) Click the 'File' tab, then click 'Open' to open the file you want to quantitate. A window will pop up named 'Bio-Format Import Options.'
(3) 'Hyperstack' and 'Colorized' options allow independent analysis of each fluorescent channel collected in the original experiment.
(4) Click on the 'Split channels' to obtain three separate windows, one for each of the three color channels, so that the quantitation of each fluorescent channel can be performed separately.
(5) Hit 'OK' at the bottom right of the window to proceed to the next quantification step.
(6) Click on the 'Freehand selections' button and then use the drawing pen to circle the area of the cell to be quantitated.
(7) Click the 'Analyze' button to select the 'Measure' option. A window will then pop up named 'Results,' which includes several measurements that the software made on the chosen area, including Median Intensity. Copy the median value in an Excel sheet for each cell measured. For example, measure 25–30 cells.

It is preferable to subtract the background Median Fluorescence Intensity (MFI) from the MFI of a region of interest (ROI) while analyzing images since the background of an image might affect the MFI quantitation.

(1) Repeat step 7 to select and measure a non-fluorescent area of the same image. MFI of that non-fluorescent area/negative control image is then subtracted from the tissue area MFI.
(2) Calculate the final MFI = MFI of an ROI – MFI of Background.
(3) Copy and paste the value in Prism to represent results in a diagram and carry out our statistical analyses.

Quantification of western blots signals

To determine the density of bands on a western blot, we used ImageJ sing the protocol reported in (https://imagej.nih.gov/ij/docs/menus/analyze.html#gels). In brief.

(1) File>Open
(2) The gel analysis routine requires the image to be a gray-scale image. To convert to grayscale, go to Image>Type>8-bit.
(3) Use the rectangular selection tool to outline the first lane. The rectangle should be tall and narrow to enclose a single road.
(4) Select *Analyze>Gels>Select First Lane* (or press "1"), and the lane will be outlined and "Lane 1 selected" displayed in the status bar.
(5) Move the rectangular selection right to the next lane and select *Analyze>Gels>Select Next Lane* (or press "2"). The designated lane is outlined and labeled, and "Lane n selected" is displayed in the status bar.
(6) Repeat the previous step for each remaining lane.
(7) Select *Analyze>Gels>Plot Lanes* (or press "3") to generate the lane profile plots.
(8) Use the straight-line selection tool to draw baselines and drop lines so that each peak of interest defines a closed area.
(9) For each peak, measure the size by clicking inside with the wand tool.
(10) Select *Analyze>Gels>Label Peaks* to label each measured peak with its size as a percent of the total length of the measured peaks.
(11) The values from the Results window can be moved to an Excel spreadsheet program to calculate the ratio between the density of a protein of interest over the density of a protein used as loading control for each sample and treatment.